Thermal hydraulic disaggregation of SMAP soil moisture over the continental United States

Pang-Wei Liu, *Member, IEEE*, Rajat Bindlish, *Senior member, IEEE*, Peggy O'Neill, *Fellow, IEEE*, Bin Fang, Venkat Lakshmi, *Senior member, IEEE*, Zhengwei Yang, *Member, IEEE*, Michael H. Cosh, *Senior member, IEEE*, Tara Bongiovanni, Chandra Holifield Collins, Patrick J. Starks, John Prueger, David D. Bosch, Mark Seyfried, and Mark R. Williams

Abstract – A Thermal Hydraulic disaggregation of Soil Moisture (THySM) algorithm was implemented to downscale NASA's Soil Moisture Active Passive (SMAP) Enhanced soil moisture (SM) product to 1 km over the continental United States (CONUS). This algorithm was developed by combining thermal inertia theory with a soil hydraulic-based approach that considers fine-scale SM spatial distribution driven by both heat fluxes and hydraulic conductivity in soils. Relative soil wetness values were estimated using land surface temperature and normalized difference vegetation index for the thermal inertia model and using soil properties for the hydraulic model. The relative soil wetness values at 1 km from both models were then combined by using weighting functions whereby the spatial distribution of SM was governed more by thermal fluxes during times of strong heat transport and infiltration during moisture abundant soil conditions. THySM values were evaluated using in situ SM measurements from SMAP Core Validation Sites (CVS), the USDA Soil Climate Analysis Network, and the NOAA Climate Reference Network over CONUS. THySM shows higher accuracy than the SMAP / Sentinel-1 (SPL2SMAP_S) 1 km SM product when compared to in situ measurements. The accuracy of THySM is 0.048 m^3/m^3 based on unbiased root mean square error (ubRMSE), outperforming SPL2SMAP_S by 0.01-0.02 m^3/m^3. The ubRMSE of THySM 1km SM over the SMAP grassland/rangeland-dominated CVS sites is better than 0.04 m^3/m^3, which meets the SMAP mission SM accuracy requirement applied at 9 and 36 km.

Index Terns– **SMAP, microwave remote sensing, soil moisture, agriculture, hydrology.**

I. INTRODUCTION

Soil moisture (SM) plays an important role in soil water and heat transport at the land surface that influences many hydrometeorological and biospherical processes [1]. Accurate SM information improves flood and drought predictions [2], [3], and provides a critical indicator for determining agricultural field activities (e.g., planting, fertilizer application, and irrigation) and valuable information for yield and production forecasts for food security [4]-[8]. Manual measurements of SM are often constrained to small domains due to the cost and intensive labor involved; however, low frequency microwave remote sensing technology, particularly at frequencies of 1-10 GHz, can provide surface SM estimates in an efficient way over large domains due to the high sensitivity of microwave measurements to changes in soil water content.

Satellite-based remote sensing missions such as the European Space Agency's (ESA) Soil Moisture and Ocean Salinity (SMOS) [9], since 2010, and the more recent National Aeronautics and Space Administration's (NASA) Soil Moisture Active Passive (SMAP) [10], since 2015, provide global SM products every 2-3 days at a spatial resolution of ~36 km. These missions operate microwave radiometers at an L-band frequency of 1.41 GHz, which is optimal for SM monitoring due to its higher sensitivity to water change deeper in soils, greater cloud and vegetation penetration capability, and higher roughness tolerance compared to other higher frequency instruments such as C- and X-band sensors [11], [12]. SMAP SM products have been used successfully in both hydrologic and agricultural applications [6], [13]-[16]. While SMAP provides wide spatial coverage and high revisit frequency, SMAP's coarse spatial resolution may not be able to provide

P.-W. Liu is with the Hydrological Sciences Laboratory at NASA Goddard Space Flight Center, Greenbelt, MD, USA, and Science Systems and Applications, Inc., Lanham, MD, USA. E-mail: pang-wei.liu@nasa.gov; R. Bindlish and P. O'Neill are with the Hydrological Sciences Laboratory at NASA Goddard Space Flight Center, Greenbelt, MD, USA; B. Fang and V. Lakshmi are with the Department of Engineering Systems and Environment at University of Virginia, Charlottesville, VA, USA; Z. Yang is with the US Department of Agriculture, National Agricultural Statistics Service, Washington DC, USA; M. Cosh is with the US Department of Agriculture, Agricultural Research Service, Hydrology and Remote Sensing Laboratory, Beltsville, MD, USA; T. Bongiovanni is with the Bureau of Economic Geology at The University of Texas at Austin, Austin, TX, USA; C. Holifield Collins is with the US Department of Agriculture, Agricultural Research Service, Southwest Watershed Research Center, Tucson, AZ, USA; P. Starks is with the US Department of Agriculture, Agricultural Research Service, Grazinglands Research Laboratory, El Reno, OK, USA; J. Prueger is with the US Department of Agriculture, Agricultural Research Service, National Laboratory for Agriculture and the Environment, Ames, IA, USA; D. Bosch is with the US Department of Agriculture, Agricultural Research Service, Southeast Experimental Watershed Research Laboratory, Tifton, GA, USA; M. Seyfried is with the US Department of Agriculture, Agricultural Research Service, Northwest Watershed Research Center, Boise, ID, USA; and M. Williams is with the US Department of Agriculture, Agricultural Research Service, National Soil Erosion Research Laboratory, West Lafayette, IN, USA.

detailed SM information that adequately accounts for heterogeneity in the domain and permits accurate estimation of terrestrial hydrometeorological processes. Previous studies suggest that flood/drought prediction and assessment may be improved by utilizing high resolution SM information [17]-[19]. SMAP SM products at ~36 km spatial resolution is also much coarser than the average size of agricultural fields in the United States (US) which is on the order of 1 km [20]. The spatial resolution of SMAP is therefore inadequate for field-scale agricultural management since the spatial distribution of SM in agricultural regions at this scale can be heterogeneous due to varying crop types, crop growth stages, and soil properties.

Various methodologies have been proposed to enhance the spatial resolution of radiometer-retrieved SM through disaggregation. Soil moisture disaggregation is based on the assumption that the spatial distribution of SM within a satellite footprint can be correlated to geophysical variables (e.g., evapotranspiration, land surface temperature, vegetation indices, soil textures, topography) at a fine scale. After building relationships between the soil water variability and geophysical parameters, the disaggregation process is conducted by maintaining the mean of disaggregated SM within a coarse scale matched to the satellite-based measurement. Disaggregation algorithms can be categorized as model-based, satellite-based, and geoinformation data-based approaches [21]. Model-based approaches typically incorporate SM at a coarse scale with either statistical [22]-[24] or physical models [25]-[29] running at a fine scale to constrain and optimize SM estimates. One of the promising approaches is to assimilate the radiometer-retrieved SM at a coarse scale into a Land Surface Model (LSM) running at a fine scale to improve SM estimates [27], [29]. These approaches require abundant geophysical and climate input information to drive models and extensive computational force when seeking estimates at a 1 km resolution across a large domain.

Satellite-based approaches utilize remotely sensed observations from either active microwave [30]-[35] or optical/thermal sensors [36]-[46] to correlate to sub-grid SM variation for the disaggregation. Given wide spatial coverage and regular revisits of many satellites, this approach is considered more applicable for large domains at near-field-size resolutions. The relationship between soil moisture and the variables from satellite observations can be built by more physically-based theory or data driven-based approaches. For example, SMAP applies radar backscattering coefficients from the European Union’s Copernicus Sentinel-1 satellites to disaggregate SMAP brightness temperature (TB) based on the high correlation between radar backscattering coefficient and radiometric brightness temperature for a given soil moisture condition. Then, SM is retrieved from fine scale TB to provide the SMAP/Sentinel-1 Level 2 SM product (SPL2SMAP_S) at 3 and 1 km [34], [35]. However, the temporal availability of this data product is reduced by ~70% due to Sentinel-1’s narrower swath and less frequent (6-12 days) satellite revisits compared to SMAP [47]. In contrast, approaches using optical/thermal sensors were developed based upon the triangle method, which correlates a tripartite relationship between land surface temperature (LST), vegetation content, and SM [48], [49]. Merlin et al. (2008 & 2012) [37], [38] developed the DISaggregation based on Physical And Theoretical scale CHange (DISPATCH) method that utilized evaporation/evapotranspiration information as a proxy for the disaggregation, while Fang et al. (2013, 2018, & 2020) [41]-[43] developed a thermal inertia model that was based on a physical relationship between changes of LST to SM for the disaggregation. Although optical/thermal data-based approaches have demonstrated their usefulness in SM disaggregation, there are often data gaps using this approach when cloud cover limits the sensor’s view of the land surface [47].

In addition to more physically-based approaches, data-driven approaches using machine learning (ML) algorithms have been developed for disaggregating SM due to their ability to capture the nonlinear relationship between SM and multiple variables [50]-[55]. For example, Srivastava et al. 2013 implemented artificial neural network (ANN), support vector machine (SVM), and relevance vector machine (RVM) algorithms with MODIS LST to disaggregate SMOS SM to demonstrate the effectiveness of the ML approaches on SM disaggregation. Nowadays, additional ML algorithms have been proposed. Liu et al., 2020 compare six of the most common ML algorithms for SM disaggregation and found that the random forest (RF) algorithm may be the most suitable approach in the ML family due to its flexibility for randomization and capability for ensemble approach.

Unlike satellite-based approaches that use dynamic remotely sensed observations, geoinformation data-based methods utilize static geophysical variables for the disaggregation process that are independent of the cloud cover and can provide data gap filling. Geoinformation data-based methods correlate SM spatial distribution to topography [56], [57] and soil attributes [58]-[60]. Across various hydro-climates and spatial scales, Gaur et al. (2016) [61] conducted a spatial statistical analysis which found that soil texture heterogeneity was the most dominant geophysical factor affecting water distribution, particularly at scales of 0.8-1.6 km. Based upon these findings, Gaur and Mohanty (2019) [60] proposed a nomograph approach for SM disaggregation that correlates the heterogeneity (using semi-variograms) of SM change to that of soil texture, in which a scaling parameter linking these two factors is a function of soil texture variability and normalized soil wetness at the coarse scale. This approach requires intensive SM measurements at fine scales to build the model; thus, it is considered applicable only in regional or catchment domains. Montzka et al. (2018) [59] utilized a first order stochastic model for gravity-driven flow derived from the Mualem-van Genuchten equation [62] that provides a closed form equation to estimate sub-grid SM variation as a function of the standard deviation of soil properties and mean SM within the coarse scale. Soil moisture disaggregation was conducted by using field capacity as the proxy to allocate water content distribution in the near-surface soil within a satellite footprint [59]. Using a more physically-based function enables this soil hydraulic approach to be implemented in a large domain; however, geoinformation data-based approaches only consider water movement effects in soils which may underestimate the impacts of surface heat transport and vegetation cover on land surface processes.

Notably, model-based, satellite-based, and geoinformation data-based methodologies have their strengths and weaknesses, and the disaggregation technique developed depends upon application goals and requirements. It is crucial to develop a SM disaggregation methodology that is able to combine approaches based upon different hypotheses to provide complementary information. In this study, we developed a thermal hydraulic disaggregation of soil moisture (THySM) algorithm to combine the thermal inertia and soil hydraulic approaches. The goal of this study is to improve the spatio-temporal resolution of SMAP SM for better applicability to hydrology and agriculture in the continental US (CONUS). We developed weighting functions, based on effective land surface heat transport rate and soil water capacity rate, to allocate contributions from the two disaggregation approaches that vary over different hydroclimatic conditions. More importantly, inclusion of the soil hydraulic approach compensates for the data gaps due to the occurrence of clouds that block LST and NDVI retrievals from satellite sensors which limits the use of the optical/thermal-based approach. Specific objectives of this study were to: 1) develop and implement THySM over CONUS, 2) validate THySM results using dense and sparse *in situ* soil moisture networks, and 3) compare the performance of THySM with SMAP/Sentinel-1 SM products at 1 km resolution. The study demonstrates the feasibility of THySM to provide consistent high spatio-temporal resolution soil moisture at reasonable accuracy for future applications.

II. SOIL MOISTURE DISAGGREGATION MODELS

A. Thermal Inertia Model

Thermal inertia is conceptually based on the hypothesis that lower heat fluxes in wet soils result in smaller LST change during the day, while dry soils experience larger LST changes. Using thermal inertia theory, Fang et al. (2013) [41] developed an approach that correlates SM to the change of LST to estimate soil wetness distribution. A linear relationship between SM and the LST difference ($\theta - \Delta T_S$) is formulated in Eq. (1):

$$\theta(i,j) = a_0 + a_1 \Delta T_s(i,j) \qquad (1)$$

where θ and ΔT_s represent the mean daily SM and the maximum difference of LST during a day at the location of (i, j), respectively, and a_0 and a_1 are two model parameters obtained using regression [41]-[43].

In our study, LST and SM from the Noah land surface model in the North American Land Data Assimilation System Phase 2 (NASA-GSFC NLDAS-2) [63] were used to build the $\theta - \Delta T_S$ relationship. Based on their corresponding Normalized Difference Vegetation Index (NDVI), LST and SM data were grouped in 0.1 increments from 0-1 (10 total groups) to represent different vegetation conditions. Although the optimal grouped value for NDVI may vary in different areas under various landcover conditions, the use of a constant value at 0.1 maintains computational efficiency for implementation in the CONUS domain, and its applicability has been demonstrated for such a domain [43][47]. The NDVI values were obtained from the NASA Land Long Term Data Record datasets (NASA-GSFC LTDR) [64]. A regression between SM and LST was conducted on a per-pixel basis and under different levels of vegetation to generate a look-up table. Soil moisture at 1 km was then estimated using high resolution LST and NDVI from Moderate Resolution Imaging Spectroradiometer (MODIS), as well as the look-up table. Land surface temperature from MODIS aboard the Aqua satellite was used because it more likely provides the maximum LST difference due to its overpass times at 1:30 AM/PM. Disaggregation was conducted to maintain the mean SM at the SMAP satellite measurement scale using Eq. (2):

$$\theta^d(i,j) = \theta(i,j) + \left[\Theta - \frac{1}{N}\sum_n \theta(i,j)\right] \qquad (2)$$

where θ^d and Θ are the disaggregated and SMAP soil moisture, respectively. This approach has previously been implemented for both watershed and continental domains [41]-[43], [47], [65], [66].

B. Soil Hydraulic-based Model

The soil hydraulic-based disaggregation was conducted using field capacity (FC) as a proxy to allocate the SM distribution within the scale of satellite measurements, as shown in Eq (3):

$$\theta^s(i,j) = \Theta + \sigma_\theta(\Theta) \cdot \frac{FC(i,j) - \overline{FC}}{\sigma_{FC}} \qquad (3)$$

where θ^s and Θ are the disaggregated SM using the soil hydraulic approach and SMAP SM, respectively [59]. $\overline{FC}$ and σ_{FC} are the mean and standard deviation of FC at the SMAP scale, respectively. The FC at fine scale was used because it can be considered as the water holding capability of soils and represents water content variability under natural drainage conditions. The FC was estimated using Mualem-van Genuchten's (MG) soil water retention and hydraulic conductivity models with soil texture properties [62]. $\sigma_\theta(\Theta)$ is the standard deviation of SM at the SMAP scale, which represents the spatial variability of soil moisture within a SMAP footprint.

Spatial variability of SM within a satellite-based observation scale is typically found to be highly correlated to the mean of SM [62], [67], [68] and may be dominated by sub-grid heterogeneity of soil properties within the satellite footprint [60], [61], [69], [70]. In hydrology, various numerical models, such as Brooks-Corey (BC) and MG models [71], [72], have been proposed to describe soil water retention and hydraulic conductivity curves for 1-dimensional (1D) unsaturated gravitational flow and transport based upon Darcy's law [62], [73]. Physically-based formulations to describe a 2D SM variation to its corresponding mean, $\sigma_\theta(\overline{\theta})$, can be derived from these models as functions of soil hydraulic properties using a stochastic analysis in a heterogeneous 2D space [62], [73], [74]. In the study, we used the formula developed from the MG model to represent the spatial variability of SM within a satellite-based observation scale (detailed mathematical formulation described in Qu et al., 2015 [62]):

$$\sigma_\theta^2(\overline{h}) = b_0^2 \left\{ \begin{matrix} b_1^2\sigma_\alpha^2 + b_2^2\left[\frac{\sigma_f^2\rho_f}{(1+a_2\rho_f)a_2} + \frac{a_1\sigma_\alpha^2\rho_\alpha}{(1+a_2\rho_\alpha)a_2} + \frac{a_3\sigma_n^2\rho_n}{(1+a_2\rho_n)a_2}\right] \\ +b_3^2\sigma_n^2 + b_4^2\sigma_{\theta_s}^2 + 2b_1b_2\left(-\frac{a_1\sigma_\alpha^2\rho_\alpha}{1+a_2\rho_\alpha}\right) \\ +2b_2b_3\left(-\frac{a_3\sigma_n^2\rho_n}{1+a_2\rho_n}\right) \end{matrix} \right\} \qquad (4)$$

where $\sigma_\theta(\overline{h})$ is the standard deviation of SM at its mean pressure head, $\overline{h}$, within a satellite observable scale and σ and ρ represent standard deviation and vertical correlation length of parameters f, α, and n, respectively. Subscripts f, α, and n are natural log-transformed saturated hydraulic conductivity ($\ln(K_s)$) and two shape parameters of the MG model, respectively. The vertical correlation lengths in surface soil are fixed at 10 cm [62]. Coefficients a_1, a_2, a_3, and b_0, b_1, b_2, b_3, and b_4 are functions of mean values of h, α, and n listed in Qu et al. (2015) [62] and Montzka et al. (2018) [59]. Hydraulic parameters f, α, and n were estimated from pedotransform equations using soil texture and chemical properties, including clay and silt fractions, bulk density, pH in H_2O, cation exchange capacity, and organic carbon content [75]. Coefficients and pedotransform equations are listed in the Appendix.

The $\sigma_\theta(\overline{h})$ in Eq. (4) can be transformed to $\sigma_\theta(\overline{\theta})$ by converting mean pressure head to mean SM using Eq. (5):

$$\overline{\theta} = \left(\overline{\theta_s} - \overline{\theta_r}\right)\left(\frac{\overline{\alpha}\overline{h}}{1+(\overline{\alpha}\overline{h})^{\overline{n}}}\right)\left(\frac{\overline{n}(\overline{\alpha}\overline{h})^{\overline{n}}+1}{\overline{n}(\overline{\alpha}\overline{h})^{\overline{n}}}\right) + \overline{\theta_r} \qquad (5)$$

where $\overline{\theta_s}$ and $\overline{\theta_r}$ are saturated and residual SM at the SMAP resolution, respectively. θ_s was set at soil porosity calculated from the bulk density dataset, and the θ_r was set at a constant 0.02 m^3/m^3, matching to the lowest available SM value from SMAP [76].

The soil hydraulic-based downscaling approach was developed based on a simple bucket theory in which the SM distribution relies on various magnitudes of infiltration due to heterogeneous soil textures. These processes may dominate water transport in the near surface soil when water content is high and thermal flux is weak as during winter seasons, cloudy days, and days with high SM content. While the approach is independent of cloud cover, it may underestimate the impacts of thermal fluxes and vegetation in regions with high surface temperature and water deficient domains.

C. Thermal Hydraulic Disaggregation Approach

In the study, a thermal hydraulic disaggregation of soil moisture (THySM) algorithm was developed. The THySM approach combines thermal inertia and soil hydraulic approaches leveraging their individual strengths and compensating for their limitations. Weighting functions based on the effective land surface heat transport rate (W_T) and soil water capacity rate (W_S) are used for the combination, formulated as:

$$\theta^{TH} = \theta^{d} \cdot \frac{W_T}{W_T+W_S} + \theta^{s} \cdot \frac{W_S}{W_T+W_S} \qquad (6\text{-}1)$$

$$W_T = \frac{LH+SH}{\{|LH|+|SH|+|GH|\}_{90PRC}} \qquad (6\text{-}2)$$

$$W_s = \begin{cases} \theta^{s}/FC; & 0 < \theta^{s} < FC \\ 1\ ; & \theta^{s} \geq FC \end{cases} \qquad (6\text{-}3)$$

where θ^{TH} is the disaggregated SM using the proposed Thermal Hydraulic (TH) approach, LH, SH, and GH are cumulated latent, sensible, and ground heat fluxes, respectively, the subscript 90PRC represents the 90th percentile of total energy flux over CONUS, and *FC* is the field capacity at 1 km. The heat flux values used to develop the W_T weighting function are provided by NLDAS-2. Although uncertainties may exist in these heat flux variables, estimates from NLDAS-2 have provided reasonable results that captured the spatial and seasonal dynamics of heat fluxes [77].

Estimation of the land surface heat transport rate, W_T (Eq. 6-2), assumes that during times of large heat transfer between the land surface and the atmosphere the SM estimate relies more on the thermal inertia approach because SM distribution may be primarily driven by heat flux processes in the soil and vegetation. In the W_T numerator, LS and SH are the two components of land surface heat fluxes that control the dynamics of the atmospheric boundary layer and largely govern water transport from the soil surface to the air [78]. LH, SH, and GH values at 1 AM-1 PM and 1 PM-1 AM were obtained from NLDAS-2 (based on the MODIS Aqua satellite's overpass times) for disaggregating SMAP SM from AM and PM half orbits, respectively. In the W_T denominator, the summation of absolute values of LH, SH, and GH represents the total energy fluxes on the land surface, regardless of their direction, and the 90th percentile of total energy flux during 2015-2020 over CONUS was used as a reference value for high heat energy condition. The 90th percentile was selected to avoid the extreme values that may result from imprecision in the NLDAS-2 model. Note must be taken that the weighting function from heat flux variables is used to indicate magnitude of impact on spatial SM distribution due to heat transport, instead of directly deriving SM. This approach relies on the relative magnitude of the heat fluxes and not on the absolute value. THySM disaggregation methodology preserves the absolute coarse resolution soil moisture estimated from remote sensing observations. Therefore, the disaggregated SM from the SMAP product is unique as compared to modeled and data assimilation estimates. In addition, the usage of public-released modeled products ensures stable and consistent data for operational purposes.

The weighting function using the soil water capacity rate, W_S (Eq. 6-3), for the soil hydraulic approach is based on the assumption that water distribution in wet soils is more strongly driven by gravitational flow as compared to in dry soils. Soil moisture was normalized by its FC to determine a relative level of wetness. The W_T and W_S were constrained between 0-1 and were normalized (Eq. 6-1) to combine the contributions from thermal inertia and hydraulic approaches. When both thermal inertia and hydraulic-derived SM were available, weighting functions were applied to apportion the impacts of thermal flux, vegetation, and infiltration on SM distribution. During cloudy days when thermal inertia-derived SM was not available, only the soil hydraulic-based approach was used to fill the gaps where the surface temperature values are not available.

III. STUDY REGION AND DATASETS

A. Study Region

This study implemented the THySM approach to enhance the spatio-temporal resolution of SMAP SM in CONUS and then evaluated its performance. Ancillary datasets used to build and implement the disaggregation processes are from land surface models and remotely sensed products. Measurements used for evaluation were obtained from nationwide *in situ* stations managed by the US Department of Agriculture (USDA), the National Oceanic and Atmospheric Administration's (NOAA) U.S. Climate Reference Network (USCRN), and the University of Texas at Austin (TxSON core site). USDA sites included both the Soil Climate Analysis Network (SCAN) and instrumented watersheds operated by the Agricultural Research Service (ARS). Figure 1 illustrates the CONUS study region and geographical distribution of the *in situ* stations. Details of the datasets are described in section III.B and summarized in TABLE I.

B. Datasets

1) Data for thermal hydraulic disaggregation: Soil moisture from the SMAP Passive Enhanced Level 2 product [76], [79], hereafter referred to as SMAP_PE, was disaggregated in the study. The SMAP_PE retrievals provide SM in the near-surface (0-5 cm) at a spatial resolution of 33 km, posted on a 9 km version of the Equal-Area Scalable Earth grid (EASE GRID 2.0). The SMAP's revisit period is 2-3 days at 6 AM or 6 PM local solar time (roughly ~1.5 days if both AM and PM orbits are used, allowing global SM monitoring at a temporal repeat of ~1.5 days).

Soil moisture (0-10 cm) and skin temperature estimates from the Noah land surface model (LSM) from NASA GSFC NLDAS-2 [63] were used to build a relationship between SM and surface temperature changes [42], [43]. The model-driven datasets provide long-term continuous data from 1979-2018 that were used to ensure a robust model and to create a reliable look up table for the thermal inertia disaggregation approach. NLDAS-2 SM and temperature were grouped based on vegetation level corresponding to 0.1 increments of NDVI data from the NASA-GSFC LTDR Advanced Very High Resolution Radiometer (AVHRR) dataset [64] in building the long-term relationship [42], [43].

Land surface temperature and NDVI at a 1 km spatial resolution from MODIS aboard the Aqua satellite (MYD11A1) [80] and on the Terra satellite (MOD13A2) [81], respectively, were used to implement the thermal inertial algorithm to disaggregate SMAP SM. Given the Aqua overpass times of 1:30 AM/PM local solar time, MYD11A1 data are more likely able to provide the nearly maximum LST change during a day. The cloud cover effect on NDVI may be lower for the Terra satellite (local overpass time of 10:30 AM/PM) compared to Aqua. In addition, the MOD13A2 provides NDVI at a 16-day temporal resolution. Therefore, when the LST is available, matching NDVI values are obtained by linear interpolation in time between the two nearest available datasets.

Soil physical (sand and clay fractions; bulk density) and chemical properties (pH in H_2O; cation exchange capacity; organic carbon content) at 1 km were used to implement the soil hydraulic-based approach [59]. The soil physical property dataset is a blended product identical to that used for the SMAP SM retrieval algorithms. Soil chemical properties were obtained from the SoilGrids database (https://soilgrids.org) managed by the International Soil Reference and Information Center [59]. Land surface energy balance components including latent, sensible, and ground heat were obtained from the Noah LSM in NLDAS-2 to estimate the effective land surface heat transfer rate for weighting SM from the thermal inertia approach. These datasets were validated using *in situ* measurements and provide reliable heat flux information in CONUS [77].

2). Data for THySM evaluation: In situ SM datasets observed at a soil depth of 5 cm from a number of SMAP Core Validation Sites (CVS), USDA SCAN, and NOAA USCRN were used to evaluate the performance of the THySM algorithm over CONUS. The CVS are intensively monitored areas approximately the size of a single SMAP footprint with multiple SM stations [82], [83] (Fig. 1). Detailed descriptions of the selected areas and their experiments have been reported previously [82], [84]-[89]. TABLE II summarizes the SM stations and climate and geophysical conditions at the CVS used in the current study. In addition, *in situ* SM data from sparse networks including SCAN [90] and USCRN [91] were used to evaluate the performance of the THySM algorithm across diverse conditions over CONUS. These sparse networks provide *in situ* SM observations distributed throughout CONUS and have been used to validate existing satellite SM missions [34], [85], [92]-[97].

IV. RESULTS AND DISCUSSION

A. Weighting Functions for THySM

Figure 2 shows normalized W_T and W_S, as used for THySM in Eq. (6-1), in different seasons across CONUS. Values over 2015-2020 were averaged in January, April, July, and October to represent winter, spring, summer, and fall seasons, respectively. As expected, normalized W_T values were lowest during winter, generally <0.2, across CONUS when the thermal fluxes were weaker (Fig. 2a). During this period, infiltration processes in near-surface soils dominate the spatial heterogeneity and are weighted higher (Fig. 2e). The THySM approach compensates for the underperformance of thermal-based approaches during winter or cold seasons [37], [42]. Normalized W_T values increased gradually throughout spring and summer when heat fluxes started to control water transport near the soil surface. In particular, higher normalized W_T values were observed in the Western US because climate-hydrological conditions are hot and dry in this region. In the Eastern US, even though strong heat fluxes occur in summer, the relatively wetter soils will exhibit non-negligible gravitational flow. During fall, the normalized W_S transitions to dominate water transport processes.

Figure 3 shows the time series of normalized W_T and W_S during 2015-2020 for two examples of 1 km x 1 km pixels near the center of South Fork, Iowa, and Walnut Gulch, Arizona. These two watersheds were selected as examples due to their differences in climate-hydrological conditions and landscapes, where the South Fork watershed is humid and dominated by cropland, and Walnut Gulch is drier (with about half of South Fork's annual rainfall) and dominated by open shrubland (TABLE II). In the South Fork watershed, normalized W_S values dominated during fall, winter, and early-spring. High values of W_S were observed from December to February because of cold soils resulting in low latent and sensible heat fluxes. As a result, THySM relied heavily on the soil hydraulic approach during this period. Normalized W_T increased as temperatures warmed during spring. Even though W_T tended to dominate W_S during summer, their separation was not obvious, with W_T = ~0.55 versus W_S = ~0.45. This pattern is likely due to the rainy season in this region extending from spring to early fall, which maintains elevated SM levels resulting in higher W_S.

Similar to the South Fork watershed, normalized W_S in Walnut Gulch dominated THySM during the winter. Because heat fluxes were non-negligible during winter in Walnut Gulch, the normalized W_T did not reach as low as in the South Fork watershed. Normalized W_T started to increase beginning in mid-January, intersected with normalized W_S in March, and then dominated the process with a value near 0.8 when hot and dry conditions began in May. The rainy season in the region starts in July; thus, the difference between W_T and W_S converged during July – October when SM was maintained at a relatively high level. During the rainy season, normalized W_T values were ~0.6, but within one day of rainfall W_S was higher than W_T indicating that the soil hydraulic approach dominated the disaggregation process during these periods following rainfall.

The weighting functions, W_T and W_S derived from heat flux variables and field capacity, respectively, were used to leverage the impacts of heat transport and water infiltration on the spatial SM distribution and for the SM disaggregation process. Such an approach is unique from modeled and data assimilation SM estimates.

B. Assessment of Thermal Hydraulic Behavior of Soil Moisture

1). Spatial analysis of THySM: The disaggregation process using the THySM approach was applied in the CONUS domain from April 1, 2015 – March 31, 2020, representing the first five years of the SMAP mission. Figure 4 shows a comparison of SM maps between SMAP_PE and SMAP_THySM for descending (AM) half orbits in the Little Washita watershed in Oklahoma from August 27 to September 10, 2017. The region is dominated by soil types of loam and silty loam in the northwest and east of the region and by sandy loam and sand in the central and southern parts of the watershed (Fig. 4a). Rainfall occurred on August 25, 2017, followed by a two-week period with no additional precipitation. Due to a 2-3 day revisit frequency, both SMAP_PE and SMAP_THySM showed soil drying (~0.30 m^3/m^3 to ~0.10 m^3/m^3) during this period (Fig. 4b1-b7 and Fig. 4c1-c7). Overall, SMAP_THySM revealed detailed SM patterns as compared to SMAP_PE. For SMAP_THySM, retrieved SM was relatively higher in the west and east of the watershed, where soils are mainly loams and silty loams. In contrast, conditions were drier in the central part of the watershed, which is dominated by sandy loam and sandy soils [98]. The higher resolution SMAP_THySM SM time-series images in Fig. 4 reflect the control imposed by soil texture on the timing of soil drying (i.e., sandier soils have lower water holding capacity than loam and silty loam soils, see Fig. 4c4 for September 2, 2017 and compare to Fig. 4a). Spatial SM patterns due to soil textural differences were not observable with SMAP_PE data due to its coarser spatial resolution. Spatial patterns of SM caused by different soil textures in the Little Washita watershed have been documented previously [98]-[100], with SM variation patterns shown in the high resolution SMAP_THySM images reinforcing these findings. The SM observed from SMAP Sentinel-1, hereafter referred to SMAP_SP, was not included in this analysis because its lower temporal revisit frequency limits its ability to observe short-term temporal SM dynamics.

A second analysis including spatial distribution of SMAP_SP SM was conducted for Walnut Gulch, Arizona. Figure 5 shows a comparison between optical images, SMAP_PE, SMAP_THySM, and SMAP_SP on May 14, 2018 and July 1, 2018, during dry and wet seasons, respectively. Land cover in the watershed is mostly open shrublands and grasslands (Fig. 5a), and is located between Mount Glenn and Mule Mountain in the north and south (Fig. 5e), respectively, which consist of closed shrublands with denser vegetation. The San Pedro River also traverses this region to the west (Fig.

5e). Overall, both high resolution SM maps from SMAP_THySM and SMAP_SP present more discernable SM features compared to the coarser resolution SMAP_PE product. The SMAP_THySM images show relatively wet SM patterns along the river and mountain areas, with SM patterns more easily observed during the rainy season in July because soils in these areas have better capability to hold water. Similar patterns can be observed with SMAP_SP, although higher variability of SM distribution was observed (partially due to noise in the Sentinel-1 radar backscatter, which potentially contributes to a wet bias in the SMAP_SP data). Additionally, a few data gaps occurred in SMAP_SP because the disaggregated brightness temperature in these pixels did not meet the retrieval quality criteria.

The spatial SM distributions of SMAP_THySM and SMAP_SP were evaluated by comparing data to *in situ* SM measurements from CVS to understand their spatial representativeness. Spatial unbiased root mean square deviations ($\mathrm{ubRMSD_{Spt}}$) of SMAP_THySM and SMAP_SP compared to *in situ* measurements were calculated on a daily basis (Eq. 7) whenever the high resolution SM products were available. For example, there are 29 *in situ* stations in Walnut Gulch, and the $\mathrm{ubRMSD_{Spt}}$ was calculated using the 29 *in situ* measurements and their corresponding 1 km SM pixels on the days when SMAP_THySM and SMAP_SP were both available. The equation for spatial unbiased root mean square deviations is:

$$ubRMSD_{Spt} = \left[\sum_{i=1}^{N}\left(\theta_{t,i} - \hat{\theta}_{t,i}\right)/N\right]^{1/2} \qquad (7)$$

where θ represents unbiased SM from either SMAP_THySM or SMAP_SP, and $\hat{\theta}$ is the *in situ* SM. Biases were considered station/location dependent and were corrected using time-series measurements from April 1, 2015 – March 31, 2020 at each station before the calculation. *i* and *t* represent the i^{th} *in situ* station at the CVS on day *t*, and *N* is the sample number on day *t*. The $\mathrm{ubRMSD_{Spt}}$ calculation was restricted by (a) requiring at least 5 available samples on the day for calculation, and (b) omitting data whenever soil temperature was lower than 4ºC to avoid freezing soils.

Figure 6 shows histograms of $\mathrm{ubRMSD_{Spt}}$ of SMAP_THySM and SMAP_SP for eight CVS. The $\mathrm{ubRMSD_{Spt}}$ of SMAP_THySM generally occurs in the lower end of the histograms (smaller $\mathrm{ubRMSD_{Spt}}$) for most sampling days during the study period. TABLE III lists the mean and standard deviation (SD) of daily $\mathrm{ubRMSD_{Spt}}$ at each CVS when both SMAP_THySM and SMAP_SP were available. SMAP_THySM shows smaller mean $\mathrm{ubRMSD_{Spt}}$ in the range of 0.035-0.061 m^3/m^3 at all CVS compared to SMAP_SP in the range of 0.041-0.076 m^3/m^3, indicating a better representative SM distribution from SMAP_THySM in these watersheds. In addition, the larger SD of $\mathrm{ubRMSD_{Spt}}$ over the study period for SMAP_SP compared to SMAP_THySM indicates more uncertain estimates of SM that may result from noise in the radar measurements due to the complex scattering mechanisms of active signals in the terrain [101]. TABLE IV lists the mean and SD of daily $\mathrm{ubRMSD_{Spt}}$ of SMAP_THySM in CVS given all available data (i.e., not just those days when SMAP_SP observations were also available), which represents the overall spatial performance of SMAP_THySM. Note that there are 4 to 9 times more days of SMAP_THySM coverage (TABLE IV) compared to concurrent SMAP_THySM and SMAP_SP coverage (TABLE III), illustrating one of the limitations of relying on only SMAP_SP data. The mean daily $\mathrm{ubRMSD_{Spt}}$ at the Walnut Gulch, Little Washita, Fort Cobb, Little River, and TxSON sites is less than or close to 0.04 m^3/m^3. The relatively larger mean daily $\mathrm{ubRMSD_{Spt}}$ (greater than or close to 0.05 m^3/m^3) at Reynolds Creek, South Fork, and St. Joseph sites may be due to complex topography and seasonally varying agricultural activities in these regions.

2). SMAP_THySM evaluation using core validation sites: In addition to spatial comparisons, performance statistics for SMAP_THySM were generated and compared with SMAP_SP using metrics of unbiased Root Mean Square Error (ubRMSE) and Correlation Coefficient (R) calculated at each 1 km SM pixel and its corresponding *in situ* station from April 1, 2015 – March 31, 2020. The ubRMSE and R of SMAP_THySM and SMAP_SP were subsequently averaged over all stations in a CVS. Figure 7 compares the validation results of SMAP_THySM and SMAP_SP products for descending (AM) and ascending (PM) half orbits for the SMAP CVS. Metrics for SMAP_PE are also included in Fig. 7 as references to evaluate the performance of the disaggregation approaches used for SMAP_THySM and SMAP_SP. It should be noted that the SMAP_PE product is at a spatial resolution of 33 km posted on a 9 km EASE2 Grid, and the statistical values were obtained from the latest SMAP assessment report, which covers the identical period as the current study [97]. Effective sample numbers used for calculating these statistics are listed in TABLE V. Statistics for SMAP_PE were not calculated for the St. Joseph watershed in the SMAP assessment report since St. Joseph, while a candidate cal/val site, is not a core validation site because the *in situ* stations are not uniformly distributed in space within the SMAP 33 km domain in the area. Even though both Sentinel-1A and -1B satellites are used for the SMAP_SP product, their low revisit frequencies (~6-12 days) and narrow swath result in low data availability in the SMAP_SP product compared to SMAP_THySM, as shown in TABLE V.

Overall, the ubRMSE and R values of SMAP_THySM at different CVS range from ~0.03 - 0.06 m^3/m^3 and ~0.6 - 0.8, respectively, outperforming those of SMAP_SP (~0.04 - 0.08 m^3/m^3 and ~0.6 – 0.7, respectively; Fig. 7). Similar results were observed for both AM and PM half orbits. Both SMAP_THySM and SMAP_SP had higher ubRMSE by about 0.015 and 0.023 m^3/m^3, respectively, compared to SMAP_PE at a resolution of 33 km. This suggests that errors from the higher resolution ancillary datasets and models may be propagated through the disaggregation process and hence increase uncertainties in the fine resolution products [38].

TABLE VI summarizes the performance statistics of SMAP_THySM using all available samples during the study period. These results are especially relevant and important for the product end users. The statistical metrics obtained from AM and PM half orbits performed similarly in ubRMSE for all the CVS with differences less than 0.002 m^3/m^3, except for South Fork. The ubRMSE statistics for Walnut Gulch, Little Washita, Fort Cobb, and TxSON were less than or equal to 0.04 m^3/m^3, which satisfies the SMAP mission SM accuracy requirement applied at 9 and 36 km. These areas are classified as open shrubland and grassland with relatively simplistic landscapes. In contrast, the ubRMSE values in intensive agricultural areas such as South Fork and St. Joseph reached as high as 0.066 m^3/m^3. This larger error may be due to the SMAP Single Channel Algorithm's (SCA) use of static vegetation and roughness parameters based on a simple land cover lookup table which is not sufficiently robust to represent changing vegetation and roughness conditions during the growing season. This results in higher errors in SMAP_PE for many agricultural areas, which can then be propagated through the disaggregation algorithm into the disaggregated SM retrieved at 1 km. In addition, the high ubRMSE observed in Reynolds Creek (~0.06 m^3/m^3) may be due to its complex hilly topography especially for a semi-arid region dominated by snowfall.

TABLE VII shows performance metrics for SMAP_THySM and SMAP_SP for the CVS when concurrent SM data were available for a comparison between the two products. Similar to the behavior of SMAP_THySM, the ubRMSE values of SMAP_SP were 0.059-0.085 m^3/m^3 in the Reynolds Creek, South Fork, and St. Joseph watersheds, relatively higher than those in other CVS with ubRMSE of 0.042 m^3/m^3 – 0.054 m^3/m^3 for both AM and PM half orbits. Because the SMAP_SP algorithm was developed based on a linear relationship between L-band brightness temperature and C-band backscattering coefficient, errors may be introduced due to radar noise, different scattering physics observed by the SMAP radiometer and Sentinel-1 radar, and mismatched overpass times between SMAP and Sentinel-1. These potential differences cannot be accurately modeled by the linear relationship used in the algorithm [47]. Therefore, additional errors may deteriorate performances of SMAP_SP in these complex landscape regions. Overall, SMAP_THySM showed lower ubRMSE values in all CVS by 0.007 m^3/m^3 to 0.015 m^3/m^3 than those from SMAP_SP for both AM and PM half orbits. In addition, the R values of SMAP_THySM were higher in all CVS by 0.03 to 0.14 compared to those of SMAP_SP. These results suggest that the thermal hydraulic disaggregation algorithm is capable of providing a more stable and reliable high resolution SM product than that from SMAP_SP.

3). THySM evaluation using sparse networks: In situ SM measurements from the USDA-SCAN and NOAA-CRN sparse networks were also used to evaluate the performance of SMAP_THySM. These selected stations, identical to those quality-controlled and used in Chen et al. (2018) [94], are well distributed over the CONUS for various landscapes and can compensate for the smaller spatial coverage of SMAP CVS. Statistical performances of SMAP_THySM and SMAP_SP are presented and compared using scatter plots with their ubRMSE and R values in Figs. 8 and 9 for AM and PM half orbits, respectively. Biases in SMAP_THySM and SMAP_SP were removed at each station using time-series measurements before plotting. Land covers of the corresponding pixels at 1 km were based on the MODIS International Geosphere-Biosphere Programme (IGBP) classification system used by the SMAP mission.

Seventy-three of 145 sparse network *in situ* stations corresponding to 1 km SM pixels were classified as grassland, while 26 stations were classified as shrubland, 26 stations as cropland, and 20 stations as crop/natural vegetation mosaic. In all, these sparse network stations provide tens of thousands of samples for

SMAP_THySM evaluation and are considered representative of their land cover categories across CONUS. SMAP_THySM values classified as grassland and shrubland performed better than cropland and crop/natural vegetation mosaic with ubRMSEs of ~0.048 and ~0.040 m^3/m^3, respectively, and Rs of ~0.78 and ~0.58, respectively. Similar to the CVS results, the sparse network pixels classified as cropland and crop/natural vegetation mosaic had greater ubRMSE (~0.06 m^3/m^3). Based on the scatter density plots, SM values concentrated at ~0.05-0.13 m^3/m^3 (yellow regions; Fig. 8, Fig. 9) for grassland and shrubland, while the SM values have a greater dynamic range between ~0.10–0.40 m^3/m^3 in the cropland and crop/natural vegetation mosaic areas. Results indicate higher dynamic soil moisture conditions in the agricultural areas, which may result from different vegetation dynamics and field practices. Therefore, these results further imply that complex vegetation and distribution negatively impact the performance of the SM retrieval and disaggregation. The statistical metrics of SMAP_THySM are summarized on TABLE VIII for both AM and PM half orbits during the study period.

The scatter density plots of SMAP_SP are also shown in Fig. 9 (e)-(h). Although similar trends can be observed in scatter plots of SMAP_SP and SMAP_THySM, a more scattered distribution of points were observed in the plots of SMAP_SP. TABLE IX lists the statistical values of SMAP_THySM and SMAP_SP using concurrent samples for AM and PM half orbits. As expected, SMAP_THySM outperformed SMAP_SP for both AM and PM half orbits in ubRMSE by ~0.01 - 0.025 m^3/m^3 and in R by ~0.1. The comparison of statistical metrics between SMAP_THySM and SMAP_SP using sparse networks presents similar performance as that using CVS. This suggests that the THySM approach for disaggregating SMAP soil moisture introduced less error as compared to the radar-based disaggregation approach. In addition, SMAP_THySM had approximately 7-10 times the amount of data availability compared to SMAP_SP, suggesting that SMAP_THySM has better applicability both in terms of accuracy and temporal frequency.

V. CONCLUSION

This study developed and implemented a Thermal Hydraulic Disaggregation of Soil Moisture (THySM) approach to disaggregate the SMAP Enhanced soil moisture (SM) product (33 km resolution, 9 km grid posting) to 1 km over the continental US. The thermal hydraulic algorithm was developed by combining thermal inertia theory with a soil hydraulic-based approach to consider SM distribution at fine spatial scale driven by both heat fluxes and infiltration under various vegetation conditions. Inclusion of the soil hydraulic approach compensates for the data gaps due to cloudy weather occurring from use of the optical/thermal-based disaggregation approach alone.

SMAP_THySM at 1 km presents a more detailed SM pattern compared to the SMAP Enhanced SM product posted on a 9 km EASE GRID and shows lower $\text{ubRMSD}_{\text{Spt}}$ than the SMAP Sentinel-1 (SMAP_SP) 1 km product over the CVS sites. The lower $\text{ubRMSD}_{\text{Spt}}$ indicates that SMAP_THySM had better spatial representativeness to SM distribution in watershed domains than SMAP_SP. Statistical time-series evaluation of SMAP_THySM resulted in a relatively low ubRMSE of ~0.04 m^3/m^3 in most grassland, rangeland, and shrubland sites, which meets the SMAP mission SM accuracy requirement applied at 9 and 36 km. However, THySM ubRMSE values in agriculture and croplands were relatively higher at ~0.06 m^3/m^3, indicating challenges for high resolution SM retrieval and disaggregation in these complex vegetative areas. Overall, SMAP_THySM outperformed SMAP_SP 1 km products in terms of accuracy and data availability, leading to advantages in hydrological applications. Presently, THySM has been ingested in the USDA NASS's Crop Condition and Soil Moisture Analytics (Crop-CASMA on https://nassgeo.csiss.gmu.edu/CropCASMA/) and is publicly available on https://portal.nccs.nasa.gov/datashare/thysm/THYSM_PM_DAILY/.

APPENDIX

Coefficients a_1, a_2, a_3, and b_0, b_1, b_2, b_3, and b_4 used for Eq. (4) are functions of mean values of h, α, and n listed in Qu et al. (2015) [62] and Montzka et al. (2018) [59].

$$a_1 = \frac{\left(\frac{5}{2}-\frac{1}{2\overline{n}}\right)\left(\overline{\alpha}\overline{h}\right)^{\overline{n}}}{1+\left(\overline{\alpha}\overline{h}\right)^{\overline{n}}}\frac{\overline{n}}{\overline{\alpha}} \qquad \text{(A1.1)}$$

$$a_2 = \frac{\left(\frac{5}{2}-\frac{1}{2\overline{n}}\right)\left(\overline{\alpha}\overline{h}\right)^{\overline{n}}}{1+\left(\overline{\alpha}\overline{h}\right)^{\overline{n}}}\frac{\overline{n}}{\overline{h}} \qquad \text{(A1.2)}$$

$$a_3 = \frac{\left(\frac{5}{2}-\frac{1}{2\overline{n}}\right)\left(\overline{\alpha}\overline{h}\right)^{\overline{n}}}{1+\left(\overline{\alpha}\overline{h}\right)^{\overline{n}}}\ln\left(\overline{\alpha}\overline{h}\right)+\frac{\ln\left(1+\left(\overline{\alpha}\overline{h}\right)^{\overline{n}}\right)}{2\overline{n}^2}-\frac{2}{\overline{n}^2-\overline{n}} \quad \text{(A1.3)}$$

and

$$b_0 = \left(\overline{\theta_s}-\overline{\theta_r}\right)\left[\frac{\overline{\alpha}\overline{h}}{\left[1+\left(\overline{\alpha}\overline{h}\right)^{\overline{n}}\right]\left(\overline{\alpha}\overline{h}\right)^{\overline{n}}\overline{n}}\right] \qquad \text{(A2.1)}$$

$$b_1 = \frac{\overline{n}\left(\overline{\alpha}\overline{h}\right)^{\overline{n}}+1-\overline{n}}{\overline{\alpha}} - \frac{\left[\overline{n}\left(\overline{\alpha}\overline{h}\right)^{\overline{n}}+1\right]\left(\overline{\alpha}\overline{h}\right)^{\overline{n}}}{1+\left(\overline{\alpha}\overline{h}\right)^{\overline{n}}}\frac{\overline{n}}{\overline{\alpha}} \qquad \text{(A2.2)}$$

$$b_2 = \frac{\overline{n}\left(\overline{\alpha}\overline{h}\right)^{\overline{n}}+1-\overline{n}}{\overline{h}} - \frac{\left[\overline{n}\left(\overline{\alpha}\overline{h}\right)^{\overline{n}}+1\right]\left(\overline{\alpha}\overline{h}\right)^{\overline{n}}}{1+\left(\overline{\alpha}\overline{h}\right)^{\overline{n}}}\frac{\overline{n}}{\overline{h}} \qquad \text{(A2.3)}$$

$$b_3 = -\frac{1}{\overline{n}} - \ln\left(\overline{\alpha}\overline{h}\right)\left[1 + \frac{\left[\overline{n}\left(\overline{\alpha}\overline{h}\right)^{\overline{n}}+1\right]\left(\overline{\alpha}\overline{h}\right)^{\overline{n}}}{1+\left(\overline{\alpha}\overline{h}\right)^{\overline{n}}}\right] \qquad \text{(A2.4)}$$

$$b_4 = \overline{n}\left(\overline{\alpha}\overline{h}\right)^{\overline{n}} + 1 \qquad \text{(A2.5)}$$

The hydraulic parameters f, α, and n in equations (A1) and (A2) are natural log-transformed saturated hydraulic conductivity ($\ln(K_s)$) and two shape parameters of the MG model, and were estimated from pedotransform equations using soil texture and chemical properties, including clay (*Cl*) and silt (*Si*) fractions, bulk density (*BD*), pH in H_2O (*pH*), cation exchange capacity (*CEC*), and organic carbon content (*OC*) [75],

$$f = \ln\left[10^{(0.0402+0.2612\times pH+0.4457\times T/S-0.0233\times Cl-0.0127\times Si-0.0104\times CEC)}\right] \qquad \text{(A3.1)}$$

$$\alpha = 10^{(-0.4335-0.4173\times BD-0.0476\times OC+0.2181\times T/S-0.0158\times Cl-0.0121\times Si)} \qquad \text{(A3.2)}$$

$$n = 10^{(0.2224-0.3019\times BD-0.0556\times T/S-0.0053\times Cl-0.0031\times Si-0.0107\times OC)} + 1 \qquad \text{(A3.3)}$$

where T/S is the top- and sub-soil distinction parameter, which is set at 1 for topsoil [75].

ACKNOWLEDGEMENTS

This study is supported by the NASA Applied Sciences and Terrestrial Hydrology programs. Authors would like to thank Dr. Fan Chen/USDA ARS for providing associated information for the USDA SCAN and NOAA CRN stations. United States Department of Agriculture (USDA) is an equal opportunity employer and provider. This research included a contribution from the Long-Term Agroecosystem Research (LTAR) network which is supported by USDA. The THySM data are available upon request by contacting corresponding authors, Dr. Pang-Wei Liu and Dr. Rajat Bindlish.

REFERENCES

[1]. J. A. Santanello Jr., P. Lawston, S. Kumar, and E. Dennis, "Understanding the impacts of soil moisture initial conditions on NWP in the context of land-atmosphere coupling," *J. Hydrometeorology*, vol. 20, no. 5, p. 793-819, doi: 10.1175/JHM-D-18-0186.1, 2019.

[2]. C. Massari, S. Camici, L. Ciabatta, and L. Brocca, "Exploiting satellite-based surface soil moisture for flood forecasting in the Mediterranean area: State update versus rainfall correction," *Remote Sens.*, vol. 10, no. 2, p. 292, doi: 10.3390/rs10020292, 2018.

[3]. T. W. Ford and S.M. Quiring, "Comparison of contemporary in situ, model, and satellite remote sensing soil moisture with a focus on drought monitoring," *Water Res. Research*, vol. 55, no. 2, p. 1565-1582, doi:10.1029/2018WR024039, 2019.

[4]. J. Judge, "Microwave remote sensing of soil water: Recent advances and issues," *Trans. ASABE*, vol. 50, no. 5, p. 1645-1649, 2007.

[5]. J. Bolten, W. T. Crow, X. Zhan, T. J. Jackson, and C. A. Reynolds, "Evaluating the Utility of Remotely Sensed Soil Moisture Retrievals for Operational Agricultural Drought Monitoring," *IEEE J. Sel. Topics Appl. Earth Observ. Remote Sens.*, vol. 3, no. 1, p. 57-66, 2010.

[6] J. Martínez-Fernández, A. González-Zamora, N. Sánchez, A. Gumuzzio, and C. M. Herrero-Jiménez, "Satellite soil moisture for agricultural drought monitoring: Assessment of the SMOD derived soil water deficit index," *Remote Sens. of Env.*, vol. 177, p. 277-286, 2016.

[7]. P.-W. Liu, T. Bongiovanni, A. Monsivais-Huertero, J. Judge, S. Steele-Dunn, R. Bindlish, and T. J. Jackson, "Assimilation of active and passive microwave observations for improved estimates of soil moisture and crop growth," *IEEE J. Sel. Topics Appl. Earth Observ. Remote Sens.*, vol. 9, no. 4, 1357-1369., 2016.

[8]. S. C. Steele-Dunne, H. McNairn, A. Monsivais-Huertero, J. Judge, P.-W. Liu, K. Papathanassiou, "Radar remote sensing of agricultural canopies: A review," *IEEE J. Sel. Topics Appl. Earth Observ. Remote Sens.*, vol. 10, no. 5, p. 2249-2273, 2017.

[9]. Y.H. Kerr, O. Waldteufel, J.-P. Wigneron, S. Delwart, F. Cabot, J. Boutin, M.-J. Escorihuela, J. Font, N. Reul, C. Gruhier, S.E. Juglea, M.R. Drinkwater, A. Hahne, M. Martin-Neira, and S. Mecklengurg, "The SMOS mission: New tool for monitoring key elements of the global water cycle," *Proc. IEEE*, vol. 98, no. 5, p. 666-687, 2010.

[10]. D. Entekhabi, E.G. Njoku, P. O'Neill, K. Kellogg, W. Crow, W Edelstein, J. Entin, S. Goodman, T.J. Jackson, J., Johnson, J. Kimball, J. Peipmeier, R. Koster, K. McDonald, M. Moghaddam, S. Moran, R. Reichle, J. Shi, M. Spencer, and S. Thurman "The soil moisture active and passive (SMAP) mission," *Proc. IEEE*, vol. 98, p. 704-716, 2010.

[11]. T.J. Jackson and T.J., Schmugge, "Vegetation effects on the microwave emission of soils," *Remote Sens. Env.*, vol. 36, no. 3, p. 203-212, 1991.

[12]. R. Bindlish, M. Cosh, T.J., Jackson, T. Koike, H. Fuji, S. Chan, J. Asanuma, A. Berg, D.D., Bosch, T. Caldwell, C. Holifield Collins, H. McNairn, J. Martínez-Fernández, J. Prueger, T. Rowlandson, M. Seyfried, P. Starks, M. Thibeault, R. Van Der Velde, J.-P. Walker, and E.J. Coopersmith, "GCOM-W AMSR2 soil moisture product validation using core validation sites," *IEEE J. Sel. Topics Appl. Earth Observ. Remote Sens.*, vol. 11, no. 1, p. 209-219, 2018.

[13]. M.-E. Ridler, H. Madsen, S. Stisen, S., Bircher, and R. Fensholt, "Assimilation of SMOS-derived soil moisture in a fully integrated hydrological and soil-vegetation-atmosphere transfer model in Western Denmark," *Water Res. Research*, vol. 55, no. 11, p. 8962-8981, doi: 10.1002/2014WR015392, 2014.

[14]. L. Brocca, T. Pellarin, W.T. Crow, L. Ciabatta, C. Massari, D. Ryu, C.-H. Su, C. Rudiger, and Y. Kerr, "Rainfall estimation by inverting SMOS soil moisture estimates: A comparison of different methods over Australia," *J. Geophys. Research: Atmos.*, vol. 121, no. 20, p. 12062-12079, doi:10.1002/2016JD025382, 2016.

[15]. R. Koster, Q. Liu, S.P.P. Mahanama, and R.H. Reichle, "Improved hydrological simulation using SMAP data: Relative impacts of model calibration and data assimilation," *J. Hydrometeorology*, vol. 19, no. 4, p. 727-741, doi: 10.1175/JHM-D-17-0228.1, 2018.

[16]. I.E. Mladenova, J.D. Bolten, W.T. Crow, N. Sazib, M.H. Cosh, and C.J. Tucker, "Evaluating the operational application of SMAP for global agricultural drought monitoring," *IEEE J. Sel. Topics Appl. Earth Observ. Remote Sens.*, vol. 12, no. 9, p. 3387-3397, doi:10.1109/JSTARS.2019.2923555, 2019.

[17]. T.J. Schmugge, W.P. Kustas, J.C. Ritchie, T.J. Jackson, and A. Rango, "Remote sensing in hydrology," *Adv. Water Res.*, vol. 25, p. 1367–1385, 2002.

[18]. M.S. Moran, C.D. Peters-Lidard, J.M. Watts, and S. McElroy, S., "Estimating soil moisture at the watershed scale with satellite-based radar and land surface models," *Canadian J. Remote Sens.*, vol. 30, no. 5, p. 805-826, 2004.

[19]. C. Dandridge, B. Fang, V. Lakshmi, "Downscaling SMAP soil moisture in the Lower Mekong River Basin," *Water*. Vol. 12, p. 56, 2019.

[20]. (2019) Farms and land in farms 2018 summary. [Online]. Available:https://www.nass.usda.gov/Publications/Todays_Reports/reports/fnlo0419.pdf.

[21]. J. Peng, A. Loew, O. Merlin, and N.E.C. Verhoest, "A review of spatial downscaling of satellite remotely sensed soil moisture," *Rev. Geophys.*, vol. 55, no. 2, p. 341-366, doi: 10.1002/2016RG000543, 2017.

[22]. Y. H. Kaheli, M.K. Gill, M.K McKee, L.A Bastidas, and E. Rosero, "Downscaling and assimilation of surface soil moisture using ground truth measurements," *IEEE Trans. Geosci. Remote Sens.*, vol. 46, no. 5, p. 1375-1384, 2008.

[23]. S. Chakrabarti, T. Bongiovanni, J. Judge, L. Zotarelli, and C. Bayer, "Assimilation of SMOS soil moisture for quantifying drought impacts on crop yield in agricultural regions," *IEEE J. Sel. Topics Appl. Earth Observ. Remote Sens.*, vol. 7, no. 9, p. 3867-3879, 2014.

[24]. S. Chakrabarti, T. Bongiovanni, J. Judge, K. Nagarajan, and J.C. Principe, "Downscaling satellite-based soil moisture in heterogeneous regions using high-resolution remote sensing products and information theory: A synthetic study," *IEEE Trans. Geosci. Remote Sens.*, vol. 53, no. 1, p. 85-101, 2014.

[25]. A. K. Sahoo, G.J. De Lannoy, R.H. Reiche, and P.R. Houser, "Assimilation and downscaling of satellite observed soil moisture over the Little River experimental watershed in Georgia, USA," *Adv. Water Res.*, vol. 52, p. 19-33, 2013.

[26]. Y. Shin, and B.P. Mohanty, "Development of a deterministic downscaling algorithm for remote sensing soil moisture footprint using soil and vegetation classifications," *Water Res. Research*, vol. 49, no. 10, p. 6208-6228, 2013.

[27]. H. Lievens, S.K. Tomers, A. Al Bitar, G. DeLannoy, M. Drusch, G., Dumedah, H.-J.H. Franssen, Y. Kerr, B. Martens, and M. Pan, "SMOS soil moisture assimilation for improved hydrologic simulation in the Murray Darling Basin, Australia," *Remote Sens. Env.*, vol. 168, p. 146-162, 2015.

[28]. A. Ebtehaj, and R.L. Bras, "A physically constrained inversion for high-resolution passive microwave retrieval of soil moisture and vegetation water content in L-band," *Remote Sens. Env.*, vol. 223, p. 111346, doi:10.1016/j.rse.2019.111346, 2019.

[29]. E. Pinnington, J. Amezcua, E. Cooper, S. Dadson, R. Ellis, J. Peng, E. Robinson, R. Morrison, S. Osborne, and T. Quaife, "Improving soil moisture prediction of a high-resolution land surface model by parameterising pedotransfer functions through assimilation of SMAP satellite data," *Hydro. Earth Sysy. Sci*, vol. 25, p. 1617-1641, 2021.

[30]. U. Narayan, V. Lakshmi, and T. Jackson, "High resolution change estimation of soil moisture using L-band radiometer and radar observations made during SMEX02 experiments," *IEEE Trans. Geosci. Remote Sens.*, vol. 44, no. 6, p. 1545-1554, 2006.

[31]. U. Narayan, and V. Lakshmi, V., "Characterizing, sub-pixel variability of low-resolution radiometer derived soil moisture using high resolution radar data," *Water Res. Research*, vol. 44, no. 6, doi: 10.1029/2006WR005817, 2008.

[32]. N. Das, D. Entekhabi, and E. Njoku, "An algorithm for merging SMAP radiometer and radar data for high-resolution soil-moisture retrieval," *IEEE Trans. Geosci. Remote Sens.*, vol. 49, no. 5, p. 1504-1512, 2011.

[33]. P.-W. Liu, J., Judge, R.D. DeRoo, A.W. England, and T. Bongiovanni, "Uncertainty in soil moisture retrievals using the SMAP combined active-passive algorithm for growing sweet corn," *IEEE J. Sel. Topics Appl. Earth Observ. Remote Sens.*, vol. 9, no. 7, p. 3326-3339, 2016.

[34]. N. Das, D. Entekhabi, R.S. Dunbar, M.J. Chaubell, A. Colliander, S. Yueh, T. Jagdhuber, F. Chen, W. Crow, P.E. O'Neill, J.P. Walker, A. Berg, D.D., Bosch, T. Caldwell, M.H. Cosh, C.H. Collins, E. Lopez-Baeza, and M. Thibeault, "The SMAP and Copernicus Sentinel-1A/B microwave active-passive high resolution surface soil moisture product," *Remote Sens. Env.*, vol. 233, doi:https://doi.org/10.1016/j.rse.2019.111380, 2019.

[35]. T. Jagdhuber, M. Baur, R. Akbar, N. Das, M. Link, L. He, and D. Entekhabi, "Estimating of active-passive microwave covariation using SMAP and Sentinel-1A data," *Remote Sens. Env.*, vol. 225, p. 458-468, 2019.

[36]. T.N. Carlson, "An overview of the triangle method for estimating surface evapotranspiration and soil moisture from satellite imagery," *Sensors*, vol. 7, no. 8, p. 1612-1629, 2007.

[37]. O. Merlin, J.P. Walker, A. Chehbouni, and Y.H. Kerr, "Toward deterministic disaggregation of SMOS soil moisture using MODIS derived soil evaporative efficiency," *Remote Sens. Env.*, vol. 112, no. 10, p. 3935-3946, 2008.

[38]. O. Merlin, C. Rudiger, A. Al Bitar, P. Richaume, J.P. Walker, and Y.H. Kerr, "Disaggregation of SMOS soil moisture in southeastern Australia," *IEEE Trans. Geosci. Remote Sens.*, vol. 50, no. 5, p. 1556-1571. 2012.

[39]. G.P. Petropoulos, T.N, Carlson, M.J., Wooster, and S. Islam, "A review of TS/VI remote sensing based methods for the retrieval of land surface energy fluxes and soil surface moisture," *Prog. Phys. Geog.: Earth and Env.*, vol. 33, no. 2, p. 224-250, doi: 10.1177/0309133309338997, 2009.

[40]. M. Piles, A. Camps, M. Vall-Llossera, I. Corbella, R. Panciera, C. Rudiger, Y.H. Kerr, and J. Walker, "Downscaling SMOS-derived soil moisture using MODIS visible/infrared data," *IEEE Trans. Geosci. Remote Sens.*, vol. 49, no. 9, p. 3156-3166, 2011.

[41]. B. Fang, V. Lakshmi, R. Bindlish, T.J. Jackson, M. Cosh, and J. Basara, "Passive microwave soil moisture downscaling using vegetation index and skin surface temperature," *Vadose Zone J.*, vol. 12, no. 3, doi:10.2136/vzj2013.05.0089, 2013.

[42]. B. Fang, V. Lakshmi, R. Bindlish, and T.J. Jackson, "Downscaling of SMAP soil moisture using land surface temperature and vegetation data,". *Vadose Zone J.*, vol. 17, p. 170198, doi:10.2136/vzj2017.11.0198, 2018.

[43]. B. Fang, V. Lakshmi, R. Bindlish, T.J. Jackson, and P.-W. Liu, "Evaluation and validation of a high spatial resolution satellite soil moisture product over the continental United States," *J. Hydrology*, vol. 588, p. 125043. https://doi.org/10.1016/j.jhydrol.2020.125043, 2020.

[44]. Y. Malbéteau, O. Merlin, B. Molero, C. Rudiger, and S. Bacon, "DisPATCc as a tool to evaluate coarse-scale remotely sensed soil moisture using localized in situ measurements: Application to SMOS and AMSR-E data in Southeastern Australia," *Int. J. Appl. Earth Observ. Geoinfo.*, vol. 45, p. 221-234, 2016.

[45]. J. Peng, A. Loew, S. Zhang, J. Wang, and J. Niesel, "Spatial downscaling of satellite soil moisture data using a vegetation temperature condition index," *IEEE Trans. Geosci. Remote Sens.*, vol. 54, no. 1, p. 558-566, 2016.

[46]. P. Abbaszadeh, H. Moradkhani, and X., Zhan, "Downscaling SMAP radiometer soil moisture over the CONUS using an ensemble learning method," *Water Res. Research*, vol. 55, p. 324-344, 2018.

[47]. P.-W. Liu, R. Bindlish, B. Fang, V. Lakshmi, P. O'Neill, Z. Yang, M.H. Cosh, T. Bongiovanni, D.D. Bosch, C. Holifield Collins, P.J. Starks, J. Prueger, M. Seyfried, and S. Livingston, "Assessing disaggregated SMAP soil moisture products in the United States," *IEEE J. Sel. Topics Appl. Earth Observ. Remote Sens.*, vol. 14, p. 2577-2592, doi: 10.1109/JSTARS.2021.3056001, 2021.

[48]. T.N. Carlson, R.R. Gillies, and T.J. Schmugge, "An interpretation of methodologies for indirect measurements of soil water content," *Agric. Forest Meteo.*, vol. 77, p. 191-205, 1995.

[49]. K. Mallick, B.K. Bhattacharya, and N.K. Patel, "Estimating volumetric surface soil moisture content for cropped soils using a soil wetness index based on surface temperature and NDVI," *Agric. Forest Meteo.*, vol. 149, p. 1327-1342, 2009.

[50]. P.K., Srivastava, D. Han, M.R. Ramirez, and T. Islam, "Machine learning techniques for downscaling SMOS satellite soil moisture using MODIS land surface temperature for Hydrological application", *Water Manag., vol. 27, p. 3127-3144, 2013.*

[51]. J. Im., S. Park, J. Rhee, J. Baik, and M. Choi, "Downscaling of AMSR-E soil moisture with MODIS products using machine learning approaches," Environ Earth. Sci., vol. 75, no. 15, p. 1-19, 2016.

[52]. E., Santi, S. Paloscia, S. Pettinato, L. Brocca, L. Giabatta, and D. Entekhabi, "On the synergy of SMAP, AMSR2 and Sentinel-1 for retrieving soil moisture," *Int. J. Appl. Earth Obs*., vol. 65, pp. 114 – 123, 2018.

[53]. W., Zhao, N. Sanchez, H. Lu, and A. Li, "A spatial downscaling approach for the SMAP passive surface soil moisture product using random forest regression", *J. Hydrology*, vol. 563, p. 1009-1024. doi:10.1016/j.hydrol.2018.06.081, 2018.

[54]. P., Abbaszadeh, H. Moradkhani, and X. Zhan, "Downscaling SMAP soil moisture over the CONUS using an ensemble learning method", *Water Res. Research*, vol. 55, p. 324-344. doi: https://doi.org/10.1029/2018WR023354, 2019.

[55]. Liu, Y., W. Jing, Q. Wang, and X. Xia, "Generating high-resolution daily soil moisture by using spatial downscaling techniques: a comparison of six machine learning algorithms", *Adv. Water Res*., vol. 141, p. 10360. doi:10.1016/j.advwatres.2020.103601, 2020.

[56]. M.L. Coleman, and J.D. Niemann, J.D., "Controls on topographic dependence and temporal instability in catchment-scale soil moisture patterns," *Water Res. Research*, vol. 49, p. 1625-1642, 2013.

[57]. K.L. Werbylo, and J.D., Niemann, "Evaluation of sampling techniques to characterize topographically-dependent variability for soil moisture downscaling," *J. Hydrology*, vol. 516, p. 304-316, 2014.

[58]. B.P. Mohanty, "Soil hydraulic property estimation using remote sensing: A review," *Vadose Zone Journal*, col. 12, vzj2013.06.0100, doi://doi.org/10.2136/vzj2013.06.0100, 2013.

[59]. C. Montzka, K. Rötzer, H. Bogena, N. Sanchez, and H. Vereecken, "A new soil moisture downscaling approach for SMAP, SMOS, and ASCAT by predicting sub-grid variability," *Remote Sens.*, vol. 10, no. 3, p. 427, 2018.

[60]. N. Gaur and B.P. Mohanty, "A nomograph to incorporate geophysical heterogeneity in soil moisture downscaling," *Water Res. Research*, vol. 55, no. 1, p. 34-54, 2019.

[61]. N. Gaur and B.P. Mohanty, "Land-surface controls on near-surface soil moisture dynamics: Traversing remote sensing footprints,". *Water Res. Research*, vol. 52, no. 8, p. 6365-6385, 2016.

[62]. W. Qu, H.R. Bogena, J.A. Huisman, J. Vanderborght, M. Schuh, E. Priesack, and H. Vereecken, H., "Predicting subgrid variability of soil water content from basic soil information," *Geophys. Res. Lett.*, vol. 42, no. 3, p. 789-796, 2015.

[63]. (2020) *Land Data Assimilation System, North American Land Data Assimilation System Phase 2 (NLDAS-2)*, [Online]. Available:https://disc.gsfc.nasa.gov/datasets?keywords=NLDAS.

[64]. "LTDR Data Products Description (Version 5 Release)," NASA Goddard Space Flight Center, Land Data Assimilation System, NASA Goddard Space Flight Center, Tech. Rep., 2017. [Online]. Available:https://ltdr.modaps.eosdis.nasa.gov/ltdr/docs/AVHRR LTDR V5 Document.pdf.

[65]. B. Fang and V. Lakshmi, "Soil moisture at watershed scale: Remote sensing techniques," *J. Hydrology*, vol. 516, p. 258-272. doi:10.1016/j.hydrol.2013.12.008, 2014.

[66]. I.P. Senanayake, I.-Y. Yeo, N. Tangdamrongsub, G.R. Willgoose, G.R. Hancock, T. Wells, B. Fang, V. Lakshmi, and J. Walker, "An in-situ data based model to downscale radiometric satellite soil moisture products in the Upper Hunter Region of NSW, Australia," *J. Hydrology*, vol. 572, p. 820-838, doi: 10.1016/j.jhydrol.2019.03.014, 2019.

[67]. J.S. Famiglietti, J.W. Rudnicki, and M. Rodell, "Variability in surface moisture content along a hillslope transect: Rattlesnack Hill, Texas," *J. Hydrology*, vol. 210, p. 259-281, 1998.

[68]. J.S. Famiglietti, D. Ryu, A.A. Berg, M. Rodell, and T.J. Jackson, "Field observations of soil moisture variability across scales," *Water Res. Research*, vol. 44, no. 1, p. W01423, doi:10.1029/2006WR005804, 2008.

[69]. T. J., Wang, T.E. Franz, V.A. Zlotnik, J.S. You, and M.D. Shulski, "Investigating soil controls on soil moisture spatial variability: Numerical simulations and field observations," *J. Hydrology*, vol. 524, p. 576–586, 2015.

[70]. J. Dong, and T.E. Ochsner, "Soil texture often exerts a stronger influence than precipitation on mesoscale soil moisture patterns," *Water Res. Research*, vol. 54, p. 2199-2211, 2018.

[71]. R.H. Brooks and A.T., Corey, "Hydraulic properties of porous media," Royal Harvard, Colorado State University, Fort Collins, 1964.

[72]. M.T. van Genuchten, "A closed-form equation for predicting the hydraulic conductivity of unsaturated soils," *Soil Sci. Soc. Am. J.*, vol. 44, no. 5, p. 892-898, 1980.

[73]. D.X. Zhang, T.C. Wallstrom, and C.L. Winter, "Stochastic analysis of steady-state unsaturated flow in heterogeneous media: Comparison of the Brooks-Corey and Gardner-Russo models," *Water Res. Research*, vol. 34, p. 1437-1449, 1998.

[74]. H. Vereecken, T. Kamai, T. Harter, R. Kasteel, J. Hopmans, and J. Vanderborght, "Explaining soil moisture variability as a function of mean soil moisture: A stochastic unsaturated flow perspective," *Geophys. Res. Lett.*, vol. 34, p. L22402, doi:10.1029/2007GL031813, 2007.

[75]. B. Tóth, M. Weynants, A. Nemes, A. Makó, G. Bilas, and G. Tóth, "New generation of hydraulic pedotransfer functions for Europe," *European J. Soil Sci.*, vol. 66, p. 226-238, doi:10.1111/ejss.12192, 2015.

[76]. P.E. O'Neill, S. Chan, E.G. Njoku, T. Jackson, R. Bindlish, and J. Chaubell, *SMAP Enhanced L2 Radiometer Half-Orbit 9 km EASE-Grid Soil Moisture, Version 4*. Boulder, Colorado USA. NASA National Snow and Ice Data Center Distributed Active Archive Center. https://doi.org/10.5067/Q8J8E3A89923, 2020.

[77]. Y. Xia, K. Mitchell, M. Ek, J. Sheffield, B. Cosgrove, E. Wood, L. Luo, C. Alonge, H. Wei, J. Meng, B. Livneh, D. Lettenmaier, V. Koren, Q. Duan, K. Mo, Y., Fan, and D. Mocko, "Continental-scale water and energy flux analysis and validation for the North American Land Data Assimilation System project phase 2 (NLDAS-2): 1. Intercomparison and application of model products," *J. Geophys. Research*. 117, D03109, doi:10.1029/2011JD016048, 2012.

[78]. B. Martens, D. Schumacher, H. Wouters, J. Munoz-Sabater, N.E.C. Verhoest, and D.G. Miralles, "Evaluating the land-surface energy partitioning in ERA5," *Geosci. Model Dev.*, vol. 13, no. 9, p. 4159-4181, doi: 10.5194/gmd-13-4159-2020.

[79]. S. Chan, R. Bindlish, P. O'Neill, T. Jackson, E. Njoku, S. Dunbar, J. Chaubell, J. Piepmeier, S. Yueh, D. Entekhabi, A. Colliander, F. Chen, M. Cosh, T. Caldwell, J. Walker, A. Berg, H. McNairn, M. Thibeault, J. Martínez-Fernández, F. Uldall, M. Seyfried, D. Bosch, P. Starks, C. Holifield Collins, J. Prueger, R. van der Velde, J. Asanuma, M. Palecki, E. Small, M. Zreda, J.-C Calvet, W. Crow, and Y. Kerr, "Development and Assessment of the SMAP Enhanced Passive Soil Moisture Product," *Remote Sens. Env.*, vol. 204, p. 931-941, doi:10.1016/j.rse.2017.08.025, 2018.

[80]. Z. Wan, S. Hook, and G. Hulley, "MYD11A1 MODIS/Aqua Land Surface Temperature/Emissivity Daily L3 Global 1km SIN Grid V006," NASA EOSDIS Land Processes DAAC, https://doi.org/10.5067/MODIS/MYD11A1.006, 2015.

[81]. K. Didan, "MOD13A2 MODIS/Terra Vegetation Indices 16-Day L3 Global 1 km SIN Grid V006," *2015*, NASA EOSDIS Land Processes DAAC, https://doi.org/10.5067/MODIS/MOD13A2.006, 2015.

[82]. E.J. Coopersmith, M.H. Cosh, P.J. Starks, D.D. Bosch, C. Holifield Collins, M. Seyfried, S. Livingston, J. Prueger, "Understanding temporal stability: a long-term analysis of USDA ARS watersheds," *Int. J. Digital Earth*, p. 1–12. doi: 10.1080/17538947.2021.1943550, 2021.

[83]. T. Bongiovanni and T.G. Caldwell, T.G., 2019. Texas soil observation network (TxSON, Texas data repository dataverse V3. https://doi.org/10.18738/T8/JJ16CF, 2019 [accessed 08 July, 2020).

[84]. T.G. Caldwell, T. Bongiovanni, M.H. Cosh, C. Halley, M.H. Young, "Field and laboratory evaluation of the CS655 soil water sensor, *Vadose Zone J.*, vol. 17, p. 170214, doi:10.2136/vzj2017.12.0214, 2018.

[85]. T.G. Caldwell, T. Bongiovanni, M.H. Cosh, T.J. Jackson, A. Colliander, C.J. Abolt, R. Casteel, T. Larson, B.R. Scanlon, M.H. Young, "The Texas soil observation network: A comprehensive, soil moisture dataset for remote sensing and land surface model validation," *Vadose Zone J.*, vol. 18, p. 190034. doi:10.2136/vzj2019.04.0034, 2019.

[86]. A. Colliander, T. Jackson, R. Bindlish, S. Chan, S. Kim, M. Cosh, S. Dunbar, L. Dang, L. Pashian, J. Asanuma, A. Berg, T. Rowlandson, D. Bosch, T. Caldwell, K. Caylor, D. Goodrich, H. al Jassar, E. Lopez-Baeza, J. Martinez-Fernandez, A. Gonzalez-Zamora, S. Livingston, H. McNairn, A. Pacheco, M. Moghaddam, C. Montzka, C. Notarnicola, G. Niedrist, T. Pellarin, J. Prueger, J. Pulliainen, K. Rautiainen, J. Ramos, M. Seyfried, P. Starks, Z. Su, Y. Zeng, R. van der Velde, M. Thibeault, W. Dorigo, M. Vreugdenhil, J Walker, X. Wu, A. Monerris, P. O'Neill, D. Entekhabi, E. Njoku, and S. Yueh, "Validation of SMAP surface soil moisture products with core validation sites," *Remote Sens. Env.*, vol. 191, p. 215-231. doi: 10.1016/j.rse.2017.01.021, 2017.

[87]. R.L. Scott, J.A., Biederman, E.P. Hamerlynck, and G.A. Barron-Gafford, "The carbon balance pivot point of southern U.S. semiarid ecosystems: Insights from the 21st century drought," *J. Geophys. Research: Biogeo.*, vol. 120, p. 2612-2624, doi: 10.1002/2015JG003181, 2015.

[88]. M.D. Murdock, D.P. Huber, M.S. Seyfried, N.R. Patton, and K.A. Lohse, CZO Dataset: Reynolds Creek Experimental Watershed - Hydropedologic Properties, Soil Water, Soil Survey (2014-2018). http://criticalzone.org/reynolds/data/dataset/6675/, 2018.

[89]. P.J. Starks, C.A. Fiebrich, D.L. Grimsley, J.D. Garbrecht, J.L. Steiner, J.A. Guzman, and D.N. Moriasi, "Upper Washita River experimental watersheds: Meteorologic and soil climate measurement networks," *J. Env. Quality*, vol. 43, p. 1239-1249, doi:10.2134/jeq2013.08.0312, 2014.

[90]. G.L. Shaefer, M.H. Cosh, and T.J. Jackson, "The USDA natural resources conservation service soil climate analysis network (SCAN)," *J. Atmos. Ocean Tech.*, vol. 24, p. 2073-2077, 2007.

[91]. J.E. Bell, M.A. Palecki, C.B. Baker, W.G. Collins, L.H. Lawrinmore, R.D. Leeper, M.E. Hall, J. Kochendorfer, T.P. Meyers, T. Wilson, and H.J. Diamond, "U.S. Climate Reference Network soil moisture and temperature observations," *J. Hydrometeorology*, vol. 14, no. 3, p. 977-988, 2013.

[92]. T.J. Jackson, M.H. Cosh, R. Bindlish, P.J. Starks, D.D. Bosch, M. Seyfried, D.C. Goodrich, M.S. Moran, and J. Du, "Validation of Advanced Microwave Scanning Radiometer Soil Moisture Products," *IEEE Trans. Geosci. Remote Sens.*, vol. 48, no. 12, p. 4256-4272, doi: 10.1109/TGRS.2010.2051035, 2010.

[93]. T.J. Jackson, R. Bindlish, M.H. Cosh, T. Zhao, P.J. Starks, D.D. Bosch, M. Seyfried, M.S. Moran, D.C. Goodrich, Y. Kerr, D. Leroux, "Validation of Soil Moisture and Ocean Salinity (SMOS) Soil Moisture Over Watershed Networks in the U.S," *IEEE Trans. Geosci. Remote Sens.*, vol. 50, no. 5, p. 1530-1543, DOI: 10.1109/TGRS.2011.2168533, 2012.

[94]. F. Chen, W.T. Crow, A. Colliander, M.H. Cosh, T.J. Jackson, R. Bindlish, R.H. Reichle, S.K. Chan, D.D. Bosch, P.J. Starks, D.C. Goodrich, and M.S. Seyfried, "Application of triple

collocation in ground-based validation of soil moisture active/passive (SMAP) Level 2 data products," *IEEE J. Sel. Topics Appl. Earth Observ. Remote Sens.*, vol. 10, no. 2, p. 489-502, 2017.

[95]. F. Chen, W.T. Crow, R. Bindlish, A. Colliander, M.S. Burgin, J. Asanuma, and K. Aida, "Global-scale evaluation of SMAP, SMOS and ASCAT soil moisture products using triple collocation," *Remote Sens. Env.*, vol. 214, p. 1-13. doi: 10.1016/j.rse.2018.05.008, 2018.

[96]. N. Das, D. Entekhabi, R.S. Dunbar, S. Kim, S. Yueh, A. Colliander, P.E. O'Neill, T. Jackson, T. Jagdhuber, F. Chen, W.T. Crow, P. O'Neill, J. Walker, A. Berg, D. Bosch, T. Caldwell, and M. Cosh, "SMAP/Sentinel-1 L2 Radiometer/Radar 30-Second Scene 3 km EASE-Grid Soil Moisture, Version 2*,"* Boulder, Colorado USA. NASA National Snow and Ice Data Center Distributed Active Archive Center. doi: https://doi.org/10.5067/KE1CSVXMI95Y, 2018.

[97]. P. O'Neill, S. Chan, R. Bindlish, M. Chaubell, A. Colliander, F. Chen, S. Dunbar, T. Jackson, J. Piepmeier, S. Misra, M. Cosh, T. Caldwell, J. Walker, X. Wu, A. Berg, T. Rowlandson, A. Pacheco, H. McNairn, M. Thibeault, J. Martínez-Fernández, Á. González-Zamora, E. Lopez-Baeza, F. Udall, M. Seyfried, D. Bosch, P. Starks, C. Holifield, J. Prueger, Z. Su, R. van der Velde, J. Asanuma, M. Palecki, E. Small, M. Zreda, J. Calvet, W. Crow, Y. Kerr, S. Yueh, and D. Entekhabi, "Calibration and validation for the L2/3_SM_P Version 7 and L2/3_SM_P_E Version 4 data products," SMAP Project, JPL D-56297, Jet Propulsion Laboratory, Pasadena, CA. https://nsidc.org/sites/nsidc.org/files/technical-references/L2_SM_P_AR_R17_Aug2020_clean_final.pdf, 2020.

[98]. T.J. Jackson, D.M. Le Vine, C.T. Swift, T.J. Schmugge, and F.R. Schiebe, " Large area mapping of soil moisture using the ESTAR passive microwave radiometer in Washita'92," *Remote Sens. Env.*, vol. 53, p. 27-37, 1995.

[99]. N.M. Mattikalli, E.T. Engman, T.J. Jackson, and L.R. Ahuja, "Microwave remote sensing of temporal variations of brightness temperature and near-surface soil water content during a watershed-scale field experiment, and its application to estimation of soil physical properties," *Water Res. Research*, vol. 34, no. 9, doi: 10.1029/98WR00553, 1998.

[100]. B.P. Mohanty and T.H. Skaggs, "Spatio-temporal evolution and time-stable characteristics of soil moisture within remote sensing footprints with varying soil, slope, and vegetation," *Adv. Water Res.*, vol. 24, p. 1051-1067, 2001.

[101]. W. Wagner, G. Bloschl, P. Pampaloni, J.C. Calvet, B. Bizzarri, J.-P. Wigneron, Y. Kerr, "Operational readiness of microwave remote sensing of soil moisture for hydrologic applications," *Hydrology Research*, vol. 38, no. 1, p. 1-20, 2007.

TABLE I
DATASETS USED IN THE STUDY

Sources	**Sensor/Model**	**Dataset**	**Spatial Resolution /Posting**	**Temporal Resolution***	**Periods**
Thermal Inertia Modeling					
NLDAS-2	Noah LSM	LST & SM	0.125°	Hourly	1981-2018
LTDR	AVHRR	NDVI	0.05°	Daily	1981-2018
Soil Hydraulic-Based Modeling					
SMAP Ancillary	Assembled product	Soil Texture	1 km	Static	Static
SoilGrid	Assembled product	Soil Chemical Properties	1 km	Static	Static
Disaggregation Implementation					
SMAP Enhanced	L-band Radiometer	SM	33 / 9 km	Daily	Apr. 2015-Mar. 2020
MODIS	Aqua	LST	1 km	Daily	Apr. 2015-Mar. 2020
MODIS	Terra	NDVI	1 km	16 days	Apr. 2015-Mar. 2020
SMAP Ancillary	Assembled product	Soil Texture	1 km	Static	Static
NLDAS-2	Noah LSM	Energy Balance (fluxes)	0.125°	Hourly	Apr. 2015-Mar. 2020
***In Situ* Measurements**					
USDA ARS	Hydra Probe	SM	Point	15-60 minutes	Apr. 2015-Mar. 2020
UT TxSON	Campbell CS655	SM	Point	Hourly	Apr. 2015-Mar. 2020
USDA SCAN	Hydra Probe	SM	Point	Hourly	Apr. 2015-Mar. 2020
NOAA USCRN	Hydra Probe	SM	Point	Hourly	Apr. 2015-Mar. 2020
Comparison					
SMAP/Sentinel-1	Radiometer & SAR	SM	1 km	Daily	Apr. 2015-Mar. 2020

*A “daily” temporal resolution refers to the availability of data somewhere in CONUS each day.

TABLE II.

CORE VALIDATION SITE INFORMATION, CLIMATE, AND GEOPHYSICAL CONDITION.

Sites	# of Stations	Area (km^2)	Annual Rainfall & Mean Temperature (mm / ºC)	Land Cover/Land Use
Walnut Gulch (WG), AZ	29	148	320 / 18	Open Shrubland/ Rangeland
Reynolds Creek (RC), ID	19	238	600 / 7	Grassland/ Rangeland
Little Washita (LW), OK	20	611	760 / 16	Grassland/ Rangeland
Fort Cobb (FC), OK	15	813	816 /16	Cropland/ Agriculture
Little River (LR), GA	29	334	1200 / 19	Woodland & Cropland/ Forest & Agriculture
South Fork (SF), IA	20	625	750 / 11	Cropland/ Agriculture
St. Joseph (StJ), IN	13	300	990 / 9	Cropland/Agriculture
TxSON (TX), TX	40	2098	807 / 18	Open Shrubland & Grassland/ Rangeland

TABLE III.
MEAN AND STANDARD DEVIATION (SD) OF DAILY UNBIASED ROOT MEAN SQUARE DEVIATION IN THE SPATIAL DOMAIN (ubRMSD$_{Spt}$) OF CONCURRENT 1 KM SMAP_THYSM AND SMAP_SP SM to *IN SITU* SOIL MOISTURE FOR THE CVS DURING APRIL 1, 2015 TO MARCH 31, 2020.

	Walnut Gulch		Reynolds Creek		Little Washita		Fort Cobb	
	THySM	SP	THySM	SP	THySM	SP	THySM	SP
Sample days	109		70		190		203	
Daily ubRMSD$_{Spt}$ mean (m^3/m^3)	0.035	0.045	0.051	0.054	0.036	0.048	0.040	0.052
SD of daily ubRMSD$_{Spt}$ (m^3/m^3)	0.018	0.024	0.020	0.029	0.014	0.028	0.014	0.019
	Little River		South Fork		St. Joseph		TxSON	
	THySM	SP	THySM	SP	THySM	SP	THySM	SP
Sample days	95		123		77		93	
Daily ubRMSD$_{Spt}$ mean (m^3/m^3)	0.045	0.052	0.061	0.076	0.047	0.057	0.035	0.041
SD of daily ubRMSD$_{Spt}$ (m^3/m^3)	0.016	0.018	0.034	0.040	0.019	0.023	0.009	0.012

TABLE IV.

MEAN AND STANDARD DEVIATION OF DAILY UNBIASED ROOT MEAN SQUARE DEVIATION IN THE SPATIAL ($\mathrm{ubRMSD_{Spt}}$) OF ALL 1 KM SMAP_THYSM SM TO *IN SITU* SOIL MOISTURE FOR THE CVS DURING APRIL 1, 2015 TO MARCH 31, 2020.

	Walnut Gulch	Reynolds Creek	Little Washita	Fort Cobb
Sample days	611	516	869	840
Daily $\mathrm{ubRMSD_{Spt}}$ mean (m^3/m^3)	0.034	0.052	0.036	0.041
SD of daily $\mathrm{ubRMSD_{Spt}}$ (m^3/m^3)	0.018	0.022	0.015	0.015

	Little River	South Fork	St. Joseph	TxSON
Sample days	885	558	554	885
Daily $\mathrm{ubRMSD_{Spt}}$ mean (m^3/m^3)	0.045	0.059	0.049	0.036
SD of daily $\mathrm{ubRMSD_{Spt}}$ (m^3/m^3)	0.017	0.031	0.020	0.011

TABLE V.
EFFECTIVE SAMPLE NUMBERS FOR CALCULATING PERFORMANCE STATISTICS FOR SMAP ENHANCED, SMAP_THYSM, AND SMAP SENTINEL-1 PRODUCTS AT SMAP CALIBRATION/VALIDATION SITES DURING APRIL 2015 – MARCH 2020.

	SMAP Enhanced (33 km posted on 9 km EASE GRID)		SMAP THySM (1 km)		SMAP Sentinel-1 (1 km)	
	AM	PM	AM	PM	AM	PM
Walnut Gulch	256	538	13448	19611	2230	1723
Reynolds Creek	170	238	7685	10998	1091	576
Little Washita	550	590	13731	13934	2990	1568
Fort Cobb	655	734	10863	11242	2234	1170
Little River	716	646	21936	21401	2118	896
South Fork	349	360	10345	10741	2192	959
St Joseph	-	-	4748	4881	613	536
TxSON	688	731	33602	34209	3195	1462

TABLE VI.

PERFORMANCE STATISTICS UNBIASED ROOT MEAN SQUARE ERROR (UBRMSE), ROOT MEAN SQUARE ERROR (RMSE), BIAS, AND CORRELATION COEFFICIENT (R) FOR SMAP THYSM PRODUCTS FOR BOTH AM AND PM HALF ORBITS DURING APRIL 1, 2015 – MARCH 31, 2020 AT SMAP CVS (ALL DATA USED).

	Walnut Gulch		Reynolds Creek		Little Washita		Fort Cobb	
	AM	PM	AM	PM	AM	PM	AM	PM
ubRMSE (m^3/m^3)	0.040	0.039	0.058	0.060	0.038	0.038	0.041	0.042
RMSE (m^3/m^3)	0.059	0.055	0.074	0.079	0.060	0.059	0.075	0.075
Bias (m^3/m^3)	0.033	0.021	-0.010	-0.021	-0.001	0.003	-0.024	-0.025
R	0.61	0.59	0.66	0.67	0.80	0.80	0.80	0.80
	Little River		South Fork		St. Joseph		TxSON	
	AM	PM	AM	PM	AM	PM	AM	PM
ubRMSE (m^3/m^3)	0.048	0.049	0.066	0.061	0.056	0.055	0.037	0.036
RMSE (m^3/m^3)	0.140	0.145	0.098	0.098	0.078	0.079	0.066	0.067
Bias (m3/m^3)	0.130	0.135	-0.062	-0.070	0.010	0.014	-0.023	-0.022
R	0.69	0.68	0.59	0.66	0.69	0.69	0.84	0.84

TABLE VII.
PERFORMANCE METRICS UNBIASED ROOT MEAN SQUARE ERROR (UBRMSE), ROOT MEAN SQUARE ERROR (RMSE), BIAS, AND CORRELATION COEFFICIENT (R) FOR CONCURRENT SMAP THYSM AND SMAP_SP PRODUCTS FOR AM AND PM HALF ORBITS DURING APRIL 1, 2015 – MARCH 31, 2020 AT SMAP CVS.

AM	Walnut Gulch		Reynolds Creek		Little Washita		Fort Cobb	
	THySM	SP	THySM	SP	THySM	SP	THySM	SP
N	2230		1091		2990		2234	
ubRMSE (m^3/m^3)	0.045	0.052	0.051	0.058	0.037	0.054	0.040	0.054
RMSE (m^3/m^3)	0.069	0.070	0.069	0.075	0.059	0.080	0.076	0.088
Bias (m^3/m^3)	0.022	0.034	-0.002	0.004	-0.001	-0.012	-0.029	-0.021
R	0.61	0.58	0.73	0.64	0.82	0.68	0.81	0.70
	Little River		South Fork		St. Joseph		TxSON	
	THySM	SP	THySM	SP	THySM	SP	THySM	SP
N	2118		2192		613		3195	
ubRMSE (m^3/m^3)	0.045	0.054	0.071	0.085	0.055	0.064	0.034	0.043
RMSE (m^3/m^3)	0.137	0.137	0.102	0.109	0.078	0.086	0.064	0.069
Bias (m3/m^3)	0.128	0.124	-0.062	-0.052	0.009	0.029	-0.028	-0.020
R	0.71	0.65	0.61	0.54	0.66	0.59	0.83	0.72
PM	Walnut Gulch		Reynolds Creek		Little Washita		Fort Cobb	
	THySM	SP	THySM	SP	THySM	SP	THySM	SP
N	1723		576		1568		1170	
ubRMSE (m^3/m^3)	0.041	0.051	0.058	0.076	0.036	0.049	0.039	0.052
RMSE (m^3/m^3)	0.058	0.065	0.079	0.095	0.058	0.077	0.075	0.088
Bias (m^3/m^3)	0.023	0.017	-0.018	-0.003	0.001	-0.008	-0.030	-0.021
R	0.65	0.52	0.73	0.53	0.78	0.65	0.78	0.69
	Little River		South Fork		St. Joseph		TxSON	
	THySM	SP	THySM	SP	THySM	SP	THySM	SP
N	896		959		536		1462	
ubRMSE (m^3/m^3)	0.046	0.052	0.064	0.081	0.064	0.065	0.033	0.042
RMSE (m^3/m^3)	0.135	0.133	0.101	0.104	0.079	0.089	0.065	0.071
Bias (m3/m^3)	0.125	0.120	-0.069	-0.060	0.014	0.035	-0.027	-0.015
R	0.71	0.68	0.59	0.52	0.72	0.64	0.84	0.72

TABLE VIII.

PERFORMANCE METRICS UNBIASED ROOT MEAN SQUARE ERROR (UBRMSE), ROOT MEAN SQUARE ERROR (RMSE), BIAS, AND CORRELATION COEFFICIENT (R) FROM SMAP THYSM SOIL MOISTURE FOR BOTH AM AND PM HALF ORBITS COMPARED TO CORRESPONDING *IN SITU* SOIL MOISTURE FROM USDA SCAN AND NOAA CRN STAIONS WHERE LANDCOVERS WERE CLASSIFIED AS GRASSLAND, SHRUBLAND, CROPLAND, AND CROP OR NATURAL VEGETAION DURING APRIL 1, 2015 – MARCH 31, 2020 (ALL DATA USED).

	Grassland		Shrubland		Cropland		Crop/Natural Veg.	
	AM	PM	AM	PM	AM	PM	AM	PM
N	40734	45356	14098	17158	13622	14852	12399	12526
ubRMSE (m^3/m^3)	0.048	0.047	0.039	0.040	0.060	0.059	0.058	0.060
RMSE (m^3/m^3)	0.065	0.066	0.053	0.054	0.091	0.092	0.089	0.092
Bias (m^3/m^3)	-0.011	-0.016	0.020	0.012	0.006	0.006	0.020	0.032
R	0.75	0.71	0.54	0.51	0.70	0.71	0.78	0.76

TABLE IX.

UNBIASED ROOT MEAN SQUARE ERROR (UBRMSE), ROOT MEAN SQUARE ERROR (RMSE), BIAS, AND CORRELATION COEFFICIENT (R) FROM CONCURRENT SMAP THYSM AND SMAP SENTINEL-1 (SP) SOIL MOISTURE PRODUCTS FOR AM AND PM HALF ORBITS COMPARED TO CORRESPONDING *IN SITU* SOIL MOISTURE FROM USDA SCAN AND NOAA CRN STAIONS WHERE LANDCOVERS WERE CLASSIFIED AS GRASSLAND, SHRUBLAND, CROPLAND, AND CROP OR NATURAL VEGETAION DURING APRIL 1, 2015 – MARCH 31, 2020.

AM	Grassland		Shrubland		Cropland		Crop/Natural Veg.	
	THySM	SP	THySM	SP	THySM	SP	THySM	SP
N	5877		2061		1741		1356	
ubRMSE (m^3/m^3)	0.047	0.055	0.039	0.044	0.057	0.081	0.052	0.061
RMSE (m^3/m^3)	0.064	0.072	0.054	0.059	0.089	0.117	0.084	0.093
Bias (m^3/m^3)	-0.008	-0.012	0.021	0.010	0.010	0.028	0.019	0.017
R	0.78	0.60	0.54	0.43	0.71	0.59	0.80	0.73
PM	Grassland		Shrubland		Cropland		Crop/Natural Veg.	
	THySM	SP	THySM	SP	THySM	SP	THySM	SP
N	3593		1331		973		636	
ubRMSE (m^3/m^3)	0.044	0.054	0.039	0.049	0.052	0.075	0.056	0.068
RMSE (m^3/m^3)	0.064	0.073	0.054	0.066	0.088	0.120	0.088	0.104
Bias (m^3/m^3)	-0.014	-0.015	0.012	0.005	-0.001	0.036	0.032	0.032
R	0.75	0.64	0.50	0.42	0.75	0.60	0.74	0.71

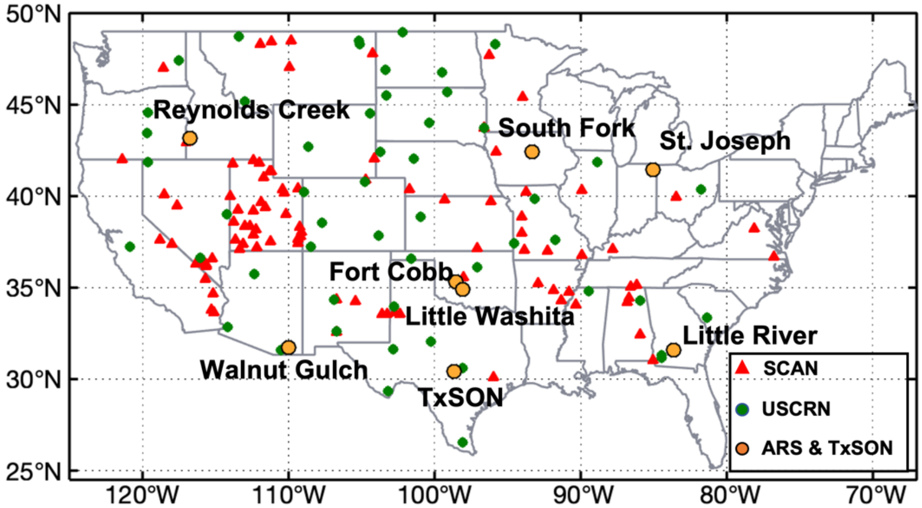

Fig. 1. Study region and *in situ* stations used for evaluating the statistical performance of soil moisture products in CONUS.

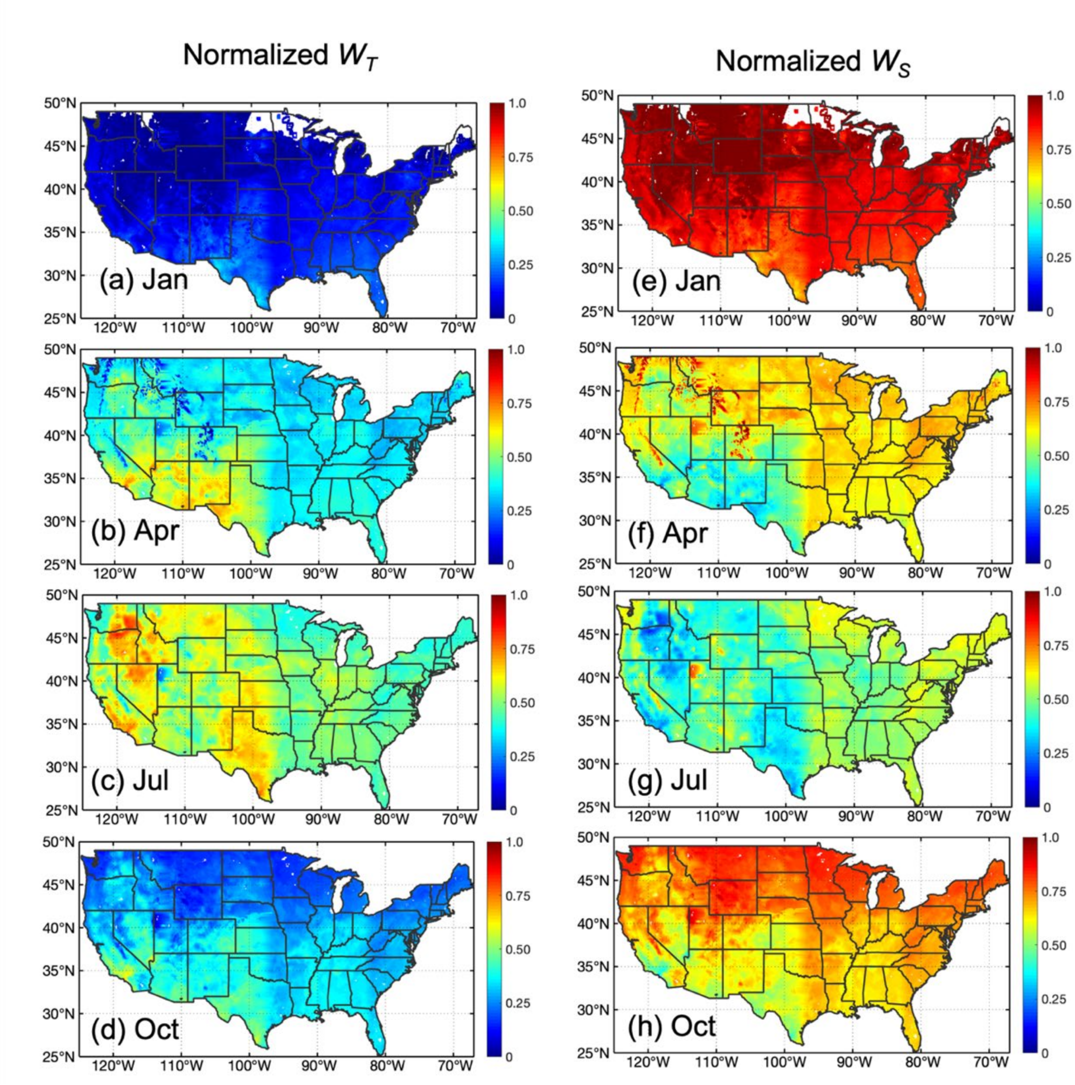

Fig. 2. Maps of normalized heat transport rate (W_T) averaged over (a) January, (b) April, (c) July, and (d) October, and normalized water capacity rate (W_S) averaged over (e) January, (f) April, (g) July, and (h) October in CONUS. These months are used to represent the winter, spring, summer, and fall seasons, respectively.

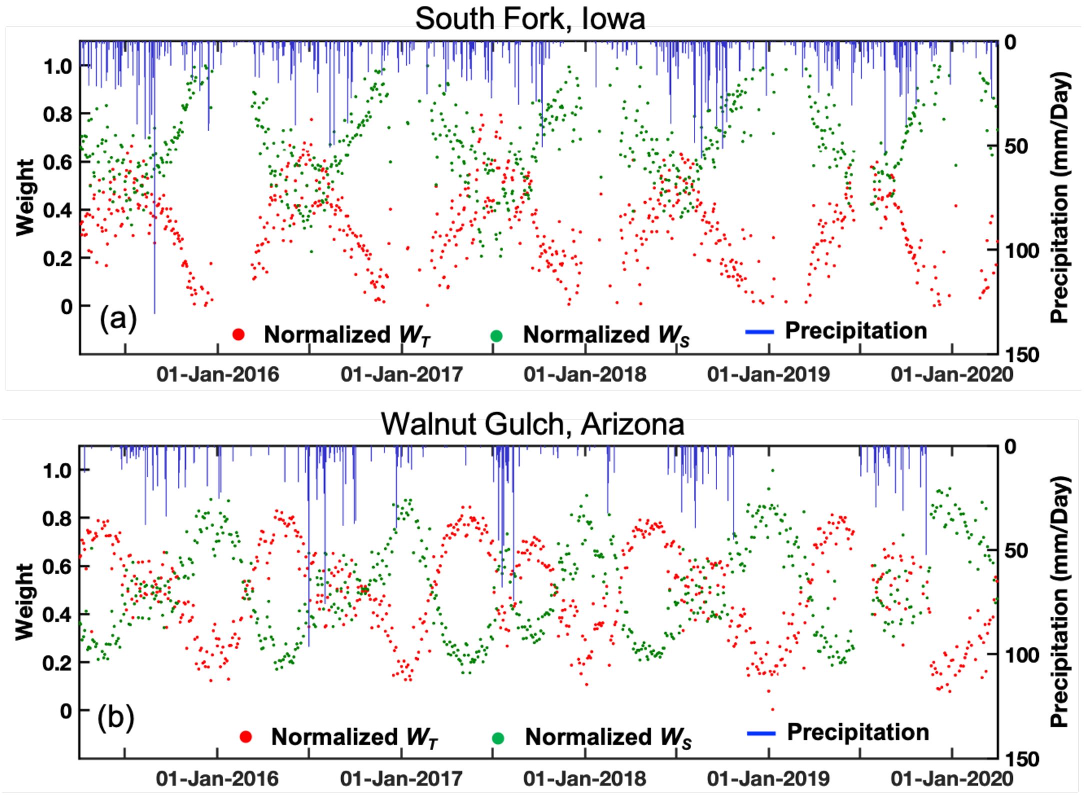

Fig. 3. Time-series variation of W_T and W_S in (a) South Fork, Iowa, and (b) Walnut Gulch, Arizona. Precipitation measurements were obtained from *in situ* rain gauges of CVS stations located in the selected pixels.

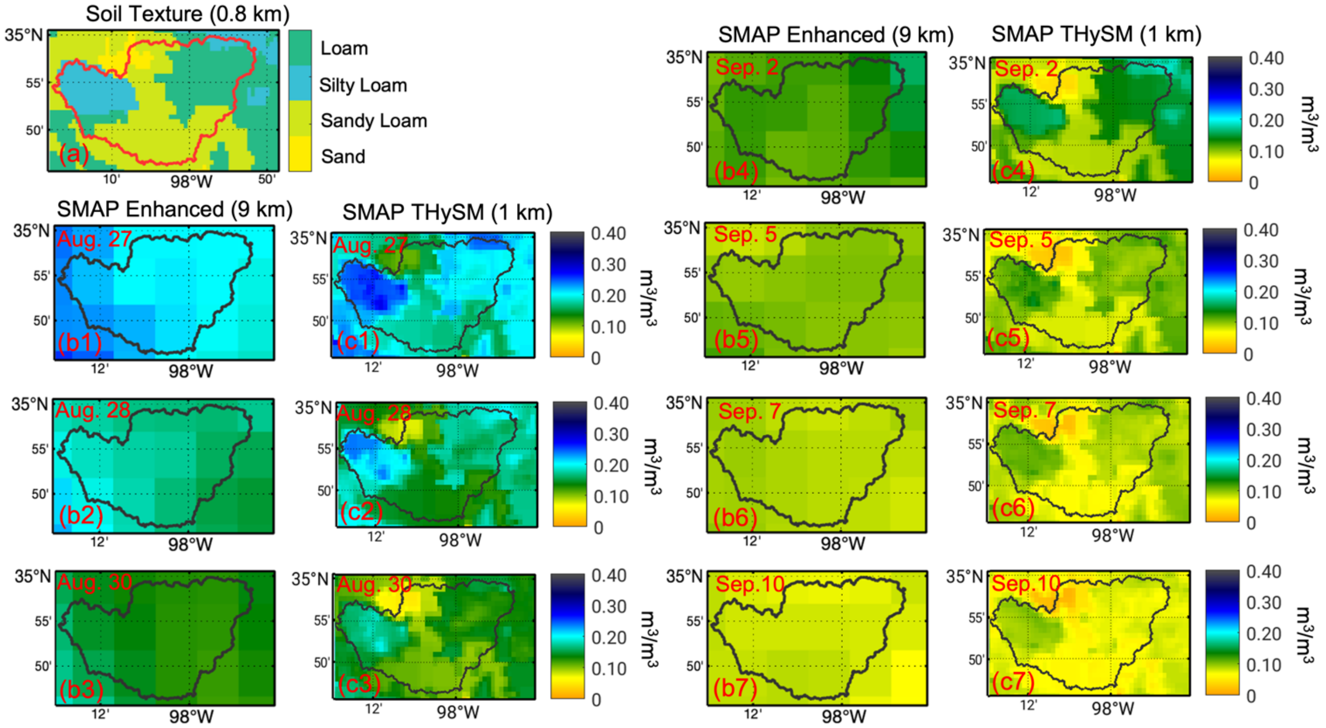

Fig. 4. (a) Soil texture classification map for Little Washita watershed, Oklahoma, where four soil classes including loam, silty loam, sandy loam, and sand are presented; sand is the predominant soil texture in the central part of the watershed while loams dominate in the west and east of the watershed; (b1) to (b7) SMAP Enhanced retrieved soil moisture during the drydown period on August 27, 28, 30, and September 2, 5, 7, and 10, 2017; (c1) to (c7) SMAP THySM retrieved soil moisture corresponding to the same days as the SMAP Enhanced product. Compared to the SMAP Enhanced soil moisture products, the SMAP THySM results more closely represent the soil moisture drydown patterns reflecting the geographical distribution of the soil texture classes (for example, compare (a) to (c4)). As expected, sandier soils dry down at a faster rate than loamy soils.

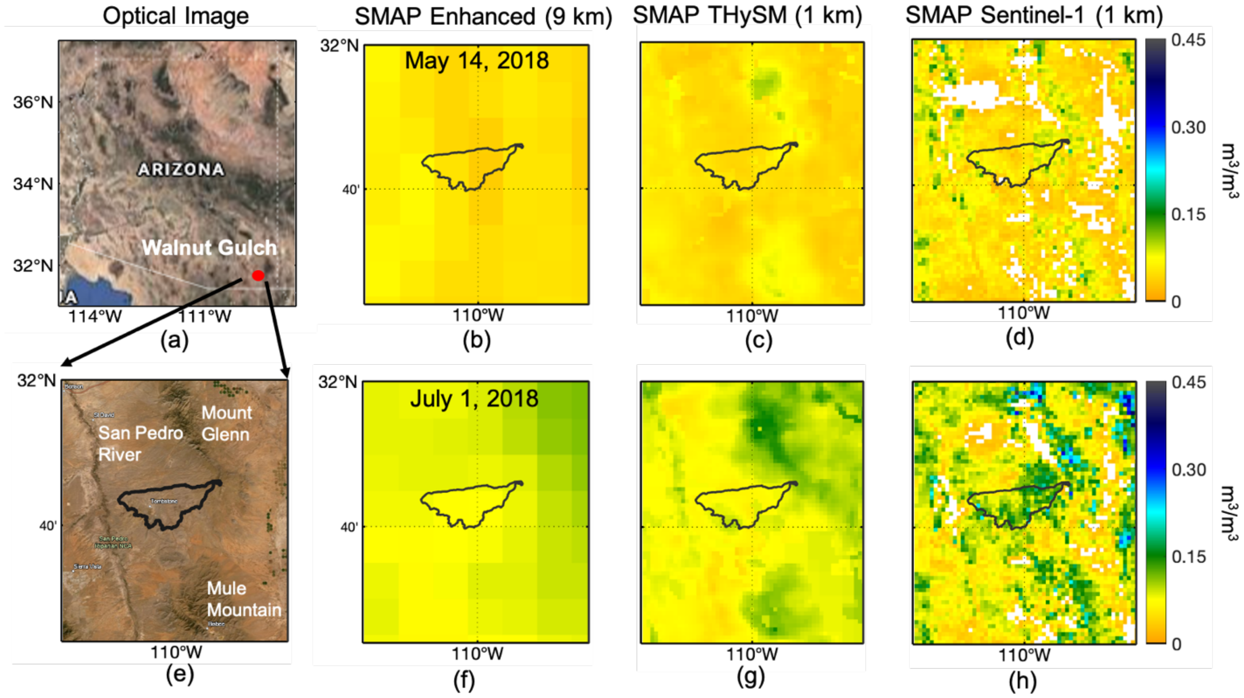

Fig. 5. (a) Optical image of Arizona and location of Walnut Gulch. Soil moisture maps in m^3/m^3 of (b) SMAP Enhanced at 9 km, (c) SMAP THySM at 1 km, and (d) SMAP Sentinel-1 at 1 km on May 14, 2018 [dry day], and (e) optical image zoomed in to Walnut Gulch; soil moisture maps of (f) SMAP Enhanced at 9 km, (g) SMAP THySM at 1 km, and (h) SMAP Sentinel-1 at 1 km on July 1, 2018 [wet day].

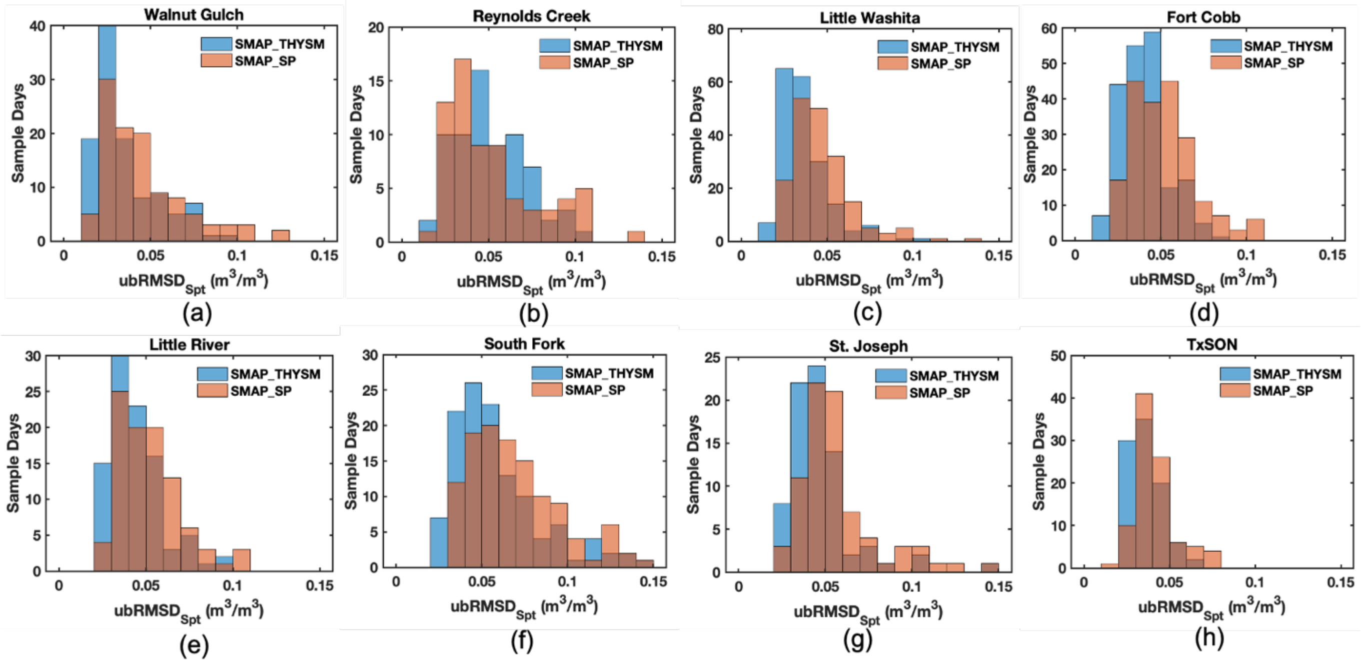

Fig. 6. Histograms of ubRMSD$_{Spt}$ of concurrent SMAP_THySM and SMAP_SP SM compared to *in situ* SM in SMAP Calibration / Validation Sites of (a) Walnut Gulch, AZ (b) Reynolds Creek, ID (c) Little Washita, OK (d) Fort Cobb, OK, (e) Little River, GA (f) South Fork, IA, (g) St. Joseph, IN and (h) TxSON, TX. The blue and pink bars represent SMAP_THySM and SMAP_SP, respectively, and the darker grey-brown color shows the overlap shadow of the two bars.

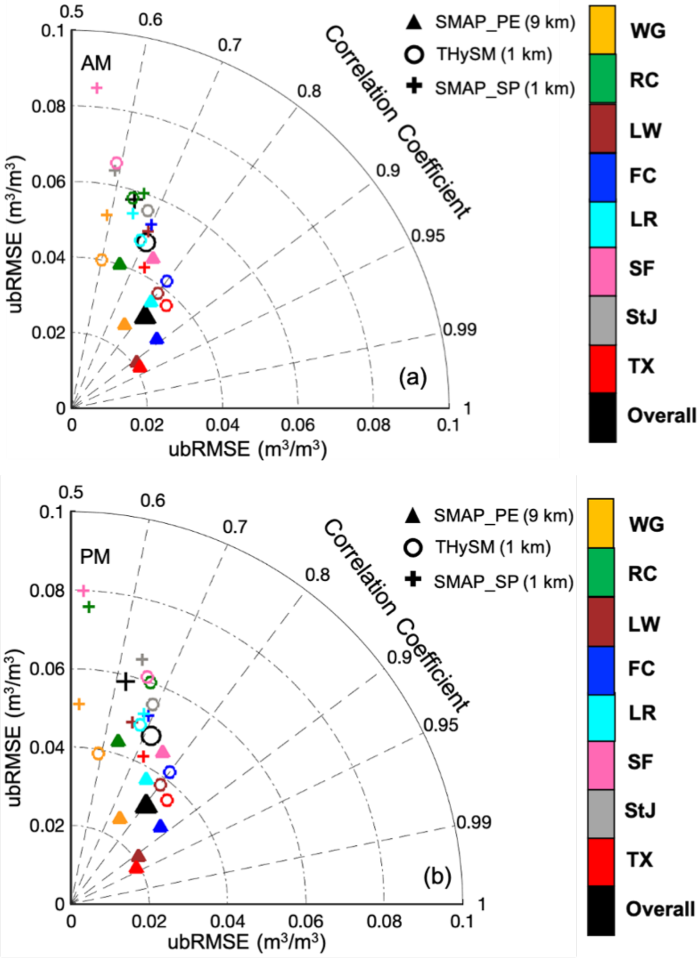

Fig. 7. Unbiased RMSE and Correlation Coefficient of SMAP_PE, SMAP_THySM and SMAP_SP soil moisture products for (a) AM and (b) PM half orbits at Calibration / Validation Sites.

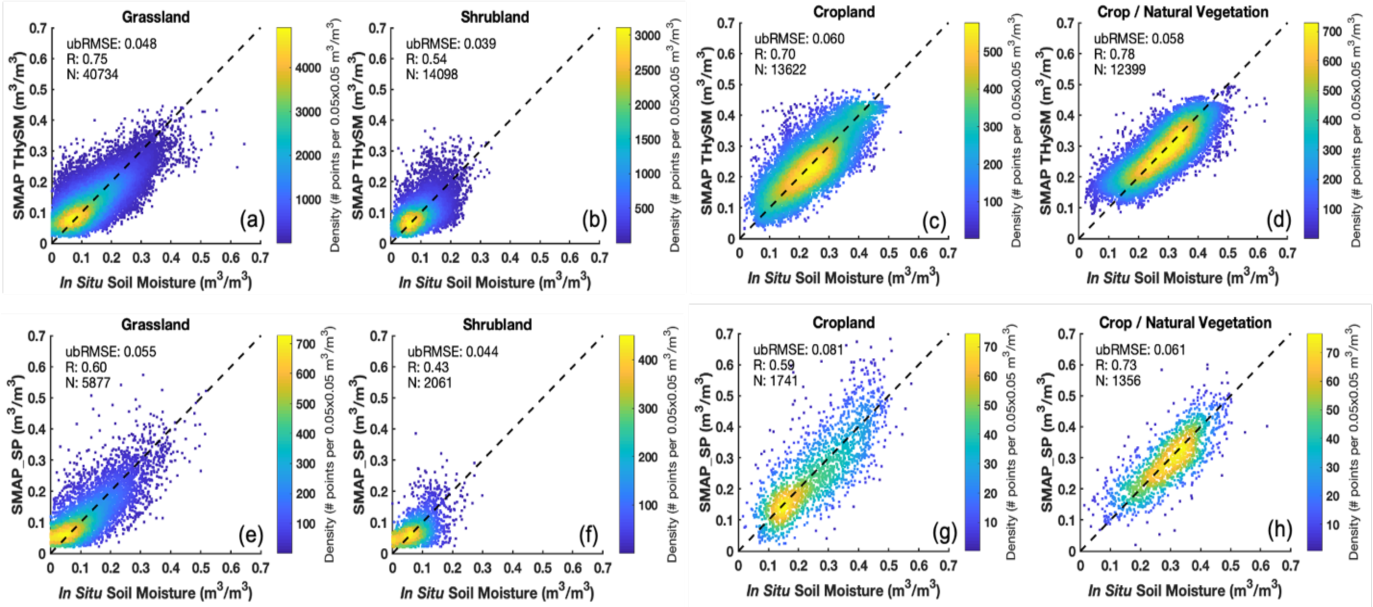

Fig. 8. Scatter density plots of *in situ* soil moisture from USDA SCAN and NOAA CRN compared to corresponding SMAP_THySM soil moisture at AM half orbits for pixels classified as landcover of (a) grassland, (b) shrubland, (c) cropland, and (d) crop and natural vegetation, and to corresponding SMAP_SP soil moisture at AM half orbits for pixels classified as landcover of (e) grassland, (f) shrubland, (g) cropland, and (h) crop and natural vegetation. Biases in SMAP_ THySM and SMAP_SP were corrected before plotting.

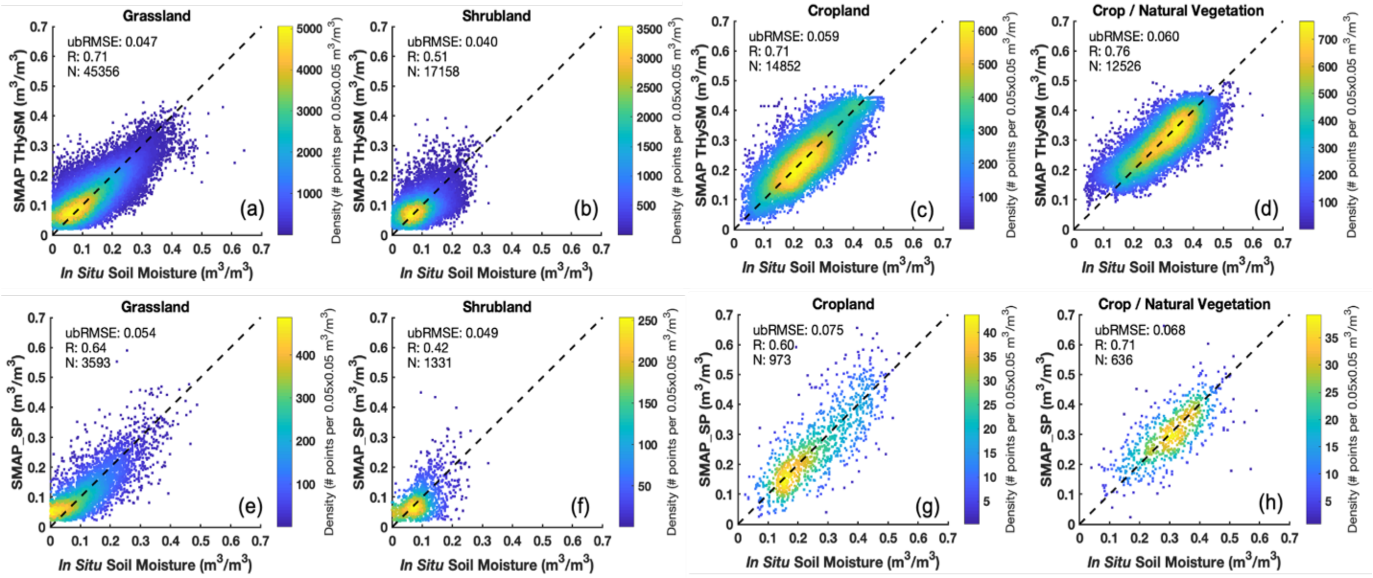

Fig. 9. Scatter density plots of *in situ* soil moisture from USDA SCAN and NOAA CRN compared to corresponding SMAP_THySM at PM half orbits for pixels classified as landcover of (a) grassland, (b) shrubland, (c) cropland, and (d) crop and natural vegetation, and to corresponding SMAP_SP at PM half orbits for pixels classified as landcover of (e) grassland, (f) shrubland, (g) cropland, and (h) crop and natural vegetation.
Biases in SMAP_THySM and SMAP_SP were corrected before plotting.